# Thermo-Mechanical behavior of hypoeutectic Ni-Y-Zr alloys

Shruti Sharma<sup>1\*</sup>, Saurabh Sharma<sup>1</sup>, Samuel Moehring<sup>1</sup>, Jun-Sang Park<sup>2</sup>, Kiran Solanki<sup>1</sup>, Pedro Peralta<sup>1</sup>

<sup>1</sup>School for Engineering of Matter, Transport, and Energy; Arizona State University, Tempe, AZ 85287, USA

<sup>2</sup> Advanced Photon Source, Argonne National Laboratory, Lemont, IL 60439, USA

#### **Abstract**

Microstructure refinement and optimized alloying can improve metallic alloy performance: stable nanocrystalline (NC) alloys with immiscible second phases, e.g., Cu-Ta, are stronger than unstable NC alloys and their coarse-grained (CG) counterparts, but higher melting point matrices are needed. Hypoeutectic, CG Ni-Y-Zr alloys were produced via arc-melting to explore their potential as high-performance materials. Microstructures were studied to determine phases present, local composition and length scales, while heat treatments allowed investigating microstructural stability. Alloys had a stable, hierarchical microstructure with ~250 nm ultrafine eutectic, ~10 μm dendritic arm spacing and ~1 mm grain size. Hardness and uniaxial compression tests revealed that mechanical properties of Ni-0.5Y-1.8Zr (in wt%) were comparable to Inconel 617 despite the small alloying additions, due to its hierarchical microstructure. Uniaxial compression at 600 °C showed that ternary alloys outperformed Ni-Zr and Ni-Y binary alloys in flow stress and hardening rates, which indicates that the Ni<sub>17</sub>Y<sub>2</sub> phase was an effective reinforcement for the eutectic, which supplemented the matrix hardening due

Email address: shruti.sharma10993@gmail.com, Phone: (623) 428-4684

<sup>\*</sup> Corresponding Author, Arizona State University, 3250 S Arizona Ave, Apt 2026, Chandler, AZ. 85248.

to increased solubility of Zr. Results suggest that ternary Ni-Y-Zr alloys hold significant promise for high temperature applications.

## **Keywords**

Nickel alloys, Thermomechanical processing, Mechanical properties, Mechanical properties (high-temperature deformation), Intermetallic compounds (IMCs), Solid solution, Ternary alloys, Zr.

### Introduction

There is a strong interest on developing new routes to increase the performance of metallic alloys used in applications that involve extreme conditions of temperature, stress, and strain rate<sup>1-4</sup>, e.g., energy generation and propulsion systems, among others<sup>5</sup>. Refinement of the length scales that control mechanical behavior using, e.g., precipitation hardening or the formation of in-situ composites where at least one phase has a very fine length scale has been particularly successful for a variety of materials, like Ni-superalloys (eutectic in the Ni-Al phase diagram)<sup>6</sup>, steel (eutectoid in the Fe-C phase diagram)<sup>7</sup>, Ti-Al alloys ( $\alpha_2 \text{ Ti}_3 \text{Al}/\gamma \text{-TiAl lamellar microstructure})^8$ , as prime examples among many others. Hierarchical microstructures have also been of major interest due to their improved mechanical properties<sup>10,11</sup>. However, all these alloy systems are reaching their upper temperature limits and alternatives with improved properties are needed. In this work, hierarchical Ni-based alloys obtained using alloying elements different from those in Nibased superalloys are studied to explore their potential for improved thermo-mechanical behavior. Nickel was chosen as the base material for this work due to its high ductility, high elastic modulus as compared to other FCC metals like Al and Cu, and relatively high melting point, thereby delaying the onset of diffusional creep mechanisms<sup>12</sup>.

Many advances have been made to improve the properties of Ni-based alloys and composites by the addition of other metals<sup>13–16</sup>. For example, Y, with no solid solubility in

Ni, but with a eutectic between pure Ni and Ni<sub>17</sub>Y<sub>2</sub>, can impart high-temperature stability to the microstructure by Y-rich precipitates<sup>17,18</sup> and the thermodynamic stability of the Ni-Y system has also been studied<sup>19-21</sup>. Zirconium, unlike Y, has some solubility in Ni, but also forms leads to a eutectic between Ni and Ni<sub>5</sub>Zr. Addition of Zr has been shown to provide better high-temperature toughness as well as refinement of the microstructure of Ni-based alloys, thus enhancing their mechanical properties<sup>22-24</sup>. Molecular dynamics simulations by Wang et al.<sup>25</sup> predict that nanoimprinted, amorphous Zr-rich Ni-Zr alloys possess improved mechanical strength as compared to Ni-rich alloys. This was supported experimentally by characterization of electrodeposited Ni/Zr-silicate composite coatings<sup>26</sup>, where Zr additions increased the hardness of the coatings. Such effects of Zr and Y additions to Ni, although promising, have not been thoroughly explored, especially at low percentages of alloy additions (below the eutectic compositions) and thus, may provide a foundation for further research.

Most engineering metallic alloys have several alloying elements, which often have synergistic interactions. Thus, the unique combination of Ni-Y-Zr was chosen at compositions suitable for the formation of intermetallic compounds (Ni<sub>17</sub>Y<sub>2</sub> and Ni<sub>5</sub>Zr that are stable up to 1300 °C) by low additions of Y and Zr in Ni, which can act as precipitates and second phases for strengthening at high temperatures as seen in Ni superalloys<sup>27,28</sup>. These two alloying elements were also chosen because Zr and Y are immiscible, which should minimize the interactions between them in ternary alloys. The Ni<sub>5</sub>Zr phase, which is FCC<sup>9,29</sup>, was found to be the stiffest amongst all the Ni-Zr intermetallic compounds from first-principle calculations<sup>30</sup> and Ni<sub>17</sub>Y<sub>2</sub> with a hexagonal structure has the highest density amongst the Ni-Y intermetallic compounds<sup>31</sup>, which tends to correlate with high strength<sup>32</sup>. Individual properties of these intermetallic compounds have also been explored in recent work to produce ultrafine ternary alloys

and other eutectic composites with Ni<sup>14,16,18</sup>, however, the Zr and Y based intermetallics have been studied separately, but not together.

For the ternary alloy system of Ni-Y-Zr, very little literature is available, especially at compositions below the eutectic in the Ni-Y and Ni-Zr alloys. Due to the immiscibility of Y in Ni, the presence of Y should be limited to the eutectic phase in Ni-Y and Ni-Y-Zr alloys. This also implies that any differences between the mechanical behavior of Ni-Zr and Ni-Y-Zr samples with the same fraction of eutectic will mostly be due to the presence of Ni<sub>17</sub>Y<sub>2</sub> in the eutectic phase. Thus, the goal of this work is to characterize the microstructure of hypoeutectic Ni-Y-Zr alloys and quantify their thermo-mechanical behavior at compositions suitable for the formation of in-situ composites with hypoeutectic and eutectic phases, thereby synthesizing a hierarchical microstructure similar to that in existing Ni superalloys.

# 1. Experimental Procedure

The Ni-Y-Zr samples were fabricated from high purity Ni, Zr and Y pieces weighed carefully to obtain the proportions required for each desired composition. The pure metal pieces were melted using a Centorr Series-5 Tri-Arc furnace equipped with a water-cooled copper hearth. The chamber of the tri-arc furnace was evacuated using an oil free vacuum pump and refilled with ultra-high purity Ar that was passed through a gas train with moisture, hydrocarbon, and oxygen filters, to further reduce contamination. The melts were solidified in the form of buttons, which were flipped and re-melted 4 to 5 times to ensure compositional and microstructural homogeneity. Low percentages of Zr and Y in the hypoeutectic range of their binary phase diagrams with Ni (1.5-2.7 wt% Zr and < 2.0 wt% Y³³) were preferred to understand the effect of alloying elements on the thermo-mechanical properties of the resulting Ni alloys, as well as to take advantage of the insolubility and small amounts of solubility of Y and Zr, respectively, in Ni to obtain

low volume fractions of the intermetallic phases, so they could act as reinforcing phases in a ductile Ni-rich matrix. Additionally, samples with compositions spanning from the hypoeutectic to the intermetallic region (0.45-15.47 wt% Y and 1.35-23.72 wt% Zr) were synthesized for comparison, as shown in Table 1.

Table 1. List of samples prepared using arc-melting, along with their assigned nomenclature.

Composition						
Ni	Zr		Y		Rationale	Nomenclature
	wt%	at%	wt%	at%		
100%	_	_	_	-	High purity Ni as reference sample	Ni
Bal	1.5	1	-	-	Low percentages of Zr (Expected ~3% Ni <sub>5</sub> Zr by volume)	1.5-Zr
Bal	2.7	1.8	-	-	Expected ~9% Ni <sub>5</sub> Zr by volume	2.7-Zr
Bal	6.3	4.2	-	-	Hypo-eutectic Ni-Zr composition	6.3-Zr
Bal	18.9	13.0	-	-	Hyper-eutectic Ni-Zr composition	18.9-Zr
Bal	20.7	14.4	-	-	Hypereutectic Ni-Zr closer to the intermetallic compositional range for Ni <sub>5</sub> Zr hardness measurement	Ni₅Zr
Bal	-	-	1.2	0.8	Similar fraction of matrix and eutectic phases as 1.5-Zr	1.2-Y
Bal	-	-	1.9	1.3	Similar fraction of matrix and eutectic phases 2.7-Zr	1.9-Y
Bal	-	-	12.3	8.5	Hyper-eutectic Ni-Y composition	12.3-Y
Bal	-	-	15.5	10.8	Hypereutectic Ni-Y for Ni <sub>17</sub> Y <sub>2</sub> hardness measurement	Ni17Y2
Bal	1.8	1.2	0.5	0.3	Ternary alloy, low Y	0.5-Y + 1.8-Zr
Bal	1.4	0.9	1.1	0.7	Ternary alloy, high Y	1.1-Y + 1.4-Zr

After arc-melting, the specimens were cross-sectioned and polished using SiC abrasive papers followed by either alumina suspensions of 5  $\mu$ m, 0.3  $\mu$ m and 0.05  $\mu$ m particle size

(for low wt% of Zr and Y in Ni) or polycrystalline diamond suspensions of 6  $\mu$ m, 3  $\mu$ m, 1  $\mu$ m and 0.25  $\mu$ m particle size (for hypereutectic and intermetallic samples). The samples were then given a final finish using a GIGA-0900 vibratory polisher with non-crystallizing colloidal silica suspension (0.02 micron) and examined using wide-angle X-ray scattering (WAXS), optical microscopy, electron backscatter diffraction (EBSD), backscattered electron (BSE) imaging, energy-dispersive X-ray spectroscopy (EDX) and wavelength dispersive X-ray spectroscopy (WDX).

The WAXS measurements were carried out at beamline 1-ID of the Advanced Photon Source (APS), Argonne National Laboratory where specimens were mounted to the sample holder in the beamline using Kapton tape and analyzed to perform preliminary structural characterization and phase identification (a description of the setup is provided by the beamline website<sup>34</sup>). Diffraction measurements were collected with a monochromatic 71.676 keV X-ray beam (λ=0.172972 Å), filtered using a Si (111) monochromator, with a beam size of 140  $\mu$ m × 140  $\mu$ m at an exposure time of 0.5 seconds for 30 frames. The detector was placed at a distance of ~ 2 m from the sample that allowed capturing data for values of 2θ between 2° and 15°. The specimens analyzed were approximately 500 µm thick, providing ~60% transmission. The Debye-Scherrer diffraction rings from the samples were recorded on a 4-panel "Hydra" detector, consisting of four GE 41RT large area detectors, each detector panel measuring 41×41 cm<sup>2</sup> and composed on a 2048 × 2048 array of 200 µm pixels<sup>35</sup>. GSAS-II software<sup>36</sup> was used for detector calibration with Cerium Oxide (CeO<sub>2</sub>), followed by integration of the specimen data to produce Intensity vs 2 $\theta$  plots. The  $\theta$  values were used to calculate the scattering vector amplitude  $q=4\pi\sin\theta/\lambda$  to analyze diffraction peaks through OriginLab software.

Optical microscopy was performed on the alloys using a Nikon Eclipse ME600 to study the microstructure of the specimens. A Tescan Vega II microscope with an accelerating voltage of 20 kV, a probe size of 350 nm, angle tilt of 70° and a hexagonal pattern with a

step size in the range of 1 to 5  $\mu$ m was used to characterize the grain size and local orientation relationships of the phases in the samples using EBSD. The elemental composition of each phase was studied using a JEOL JXA-8530F electron microprobe (EPMA) via BSE imaging (15 keV energy and 15 nA current), EDX (15 kV voltage, 30 nA current, 100 seconds acquisition time and 7000 CPS count rate) and WDX analysis to confirm the expected phases and quantify overall composition. WDX was used due to the low percentages of Y present and the small difference between the energy levels of Zr and Y<sup>37-39</sup>. For WDX analysis, a beam size of 1  $\mu$ m was used for better resolution and spot analysis was done at various points on the different phases using a moderate excitation voltage of 15 kV (~2xK $\alpha$  Ni = 2x7.471 keV; for Zr and Y, L $\alpha$  was used, which is 1.9922 keV for Y and 2.042 keV for Zr<sup>37</sup>) with a beam current of 100 nA. An average of the values was then taken to estimate the concentration of Zr and Y in each phase. Images collected in BSE mode were further analyzed using image processing software (ImageJ<sup>40</sup>) to evaluate different length scales present in the microstructure, e.g., the average lamellar thickness ( $\lambda$ t) of the eutectic phase, and to quantify phase percentage.

To evaluate the microstructural stability at high temperatures, the specimens were heat-treated at 1100 °C, just below the eutectic temperature of Ni-Zr, i.e., 1170 °C. Note that eutectic temperature of Ni-Y is 1285 °C, thus the value for Ni-Zr was used as an upper bound to avoid phase changes. The heat treatment lasted for 2 hours and was carried out in an inert Ar-5%H<sub>2</sub> atmosphere. Argon with 5%H<sub>2</sub> was used because hydrogen would prevent any formation of oxides, and it was present in small enough quantities (5%) to avoid forming hydrides with Zr or Y present in the alloys<sup>41,42</sup>. Samples were water-quenched to preserve the annealed microstructure.

Quantification of mechanical behavior of the alloys was performed using micro-hardness and uniaxial compression testing. Vickers hardness was measured using a Leco micro-hardness indenter with 500 g load with a 15 second dwell time. This load was decided to

ensure that the size of the Vickers indent is large enough to account for the combined effect of the eutectic and matrix to evaluate the hardness of the alloy before and after heat treatment. A 300 g load was used to evaluate the hardness of Ni<sub>5</sub>Zr and 200 g for Ni<sub>17</sub>Y<sub>2</sub> samples as the lower load allowed to probe individual phases more easily. Furthermore, uniaxial compression testing was performed at room temperature (RT) and 600 °C in air using an Instron servo-hydraulic load frame, equipped with a load cell of 50 kN (11 kips) capacity. Inconel 718 rods with WC platens were used along with lithium-based RENOLIT ST-80 grease at room temperature and Lub-O-Seal® NM-91<sup>TM</sup> Anti-Seize grease at high temperature. The samples were prepared in the form of parallelepipeds with height to length ratio between 1 to 2 as per ASTM standards<sup>43</sup> with top and bottom faces polished up to 1200 SiC grit finish. The flat ends and the grease prevented barreling of the specimens. The compression tests were performed under displacement control, at a constant strain rate of 0.005mm/mm/min<sup>43,44</sup>.

#### 2. Results

## 2.1 Structural and microstructural characterization

The WAXS measurements performed on the various compositions of binary and ternary alloys mentioned in Table 1 revealed the constituent phases as shown in Figure 1.

The raw diffraction patterns consisting of Debye-Scherrer rings for both binary and ternary alloys (refer to Fig. 1S of the supplementary information) for one quadrant were similar for all panels of the Hydra detector. After finding the pattern center and calibrating the relationship between the radial position of a diffraction ring and the corresponding value of  $2\theta$ , the 2D patterns were then integrated to obtain 1D line profiles as shown in Figure 1 with I(q) as the scattered intensity at a given value of the scattering vector amplitude q.

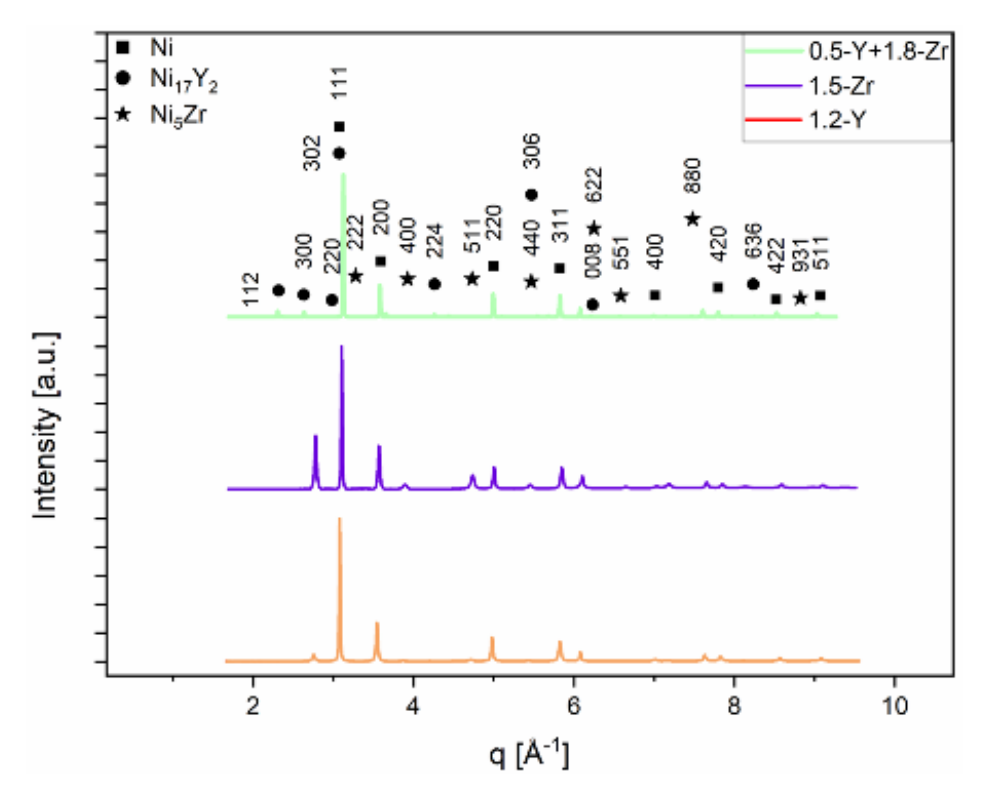


Figure 1. Integrated diffraction pattern from WAXS analysis of arc-melted Ni-Y, Ni-Zr and Ni-Y-Zr alloys of different compositions.

Figure 1 indicates the presence of FCC Ni, along with FCC Ni<sub>5</sub>Zr and hexagonal Ni<sub>17</sub>Y<sub>2</sub> phases in arc-melted specimens, in accordance with the phase diagrams<sup>33</sup> and literature<sup>30,31,33,45,46</sup>. The crystal planes were matched with the ideal crystals of Ni, Ni<sub>5</sub>Zr and Ni<sub>17</sub>Y<sub>2</sub> obtained from the Materials Project website<sup>47</sup> and their corresponding diffraction patterns calculated using CrystalDiffract<sup>TM</sup> software<sup>48</sup>. The confirmation of the expected phases allowed a better interpretation of the EBSD and optical microscopy results, as described next.

The microstructures of arc melted samples studied using optical microscopy were found to be as expected from their compositions and the corresponding binary phase diagrams<sup>33</sup>, i.e., hypoeutectic, dendritic microstructures. Characterization using EBSD quantified the grain size and complemented the observations from optical microscopy. Examples of data collected for samples of Ni+2.7 wt% Zr and Ni+1.1 wt% Y + 1.4 wt% Zr are shown in Figure 2.

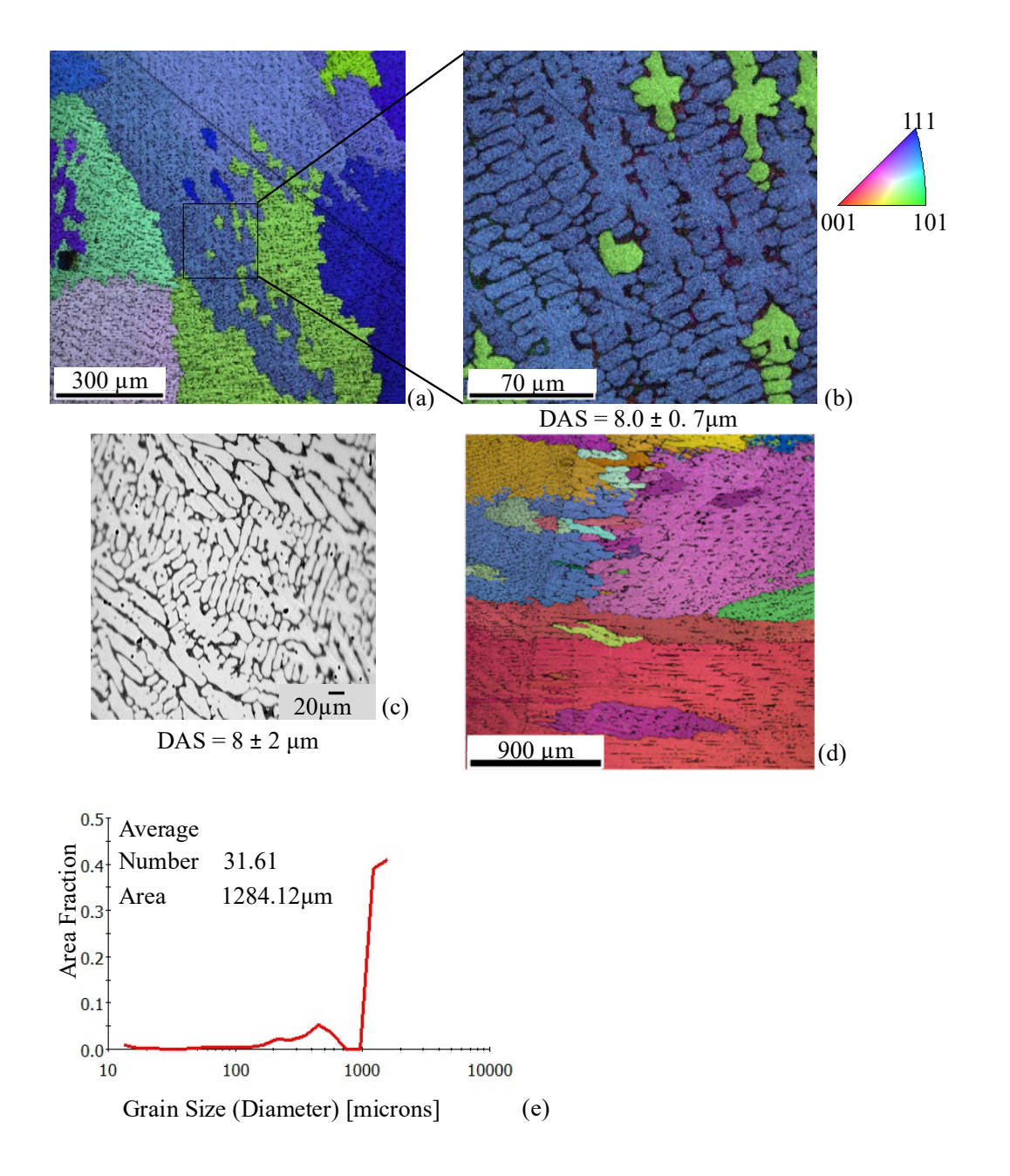


Figure 2. Microstructure images obtained via EBSD and optical microcopy from 2.7-Zr and 1.1-Y + 1.4-Zr: (a) Low magnification inverse pole figure (IPF) with superimposed image quality (IQ) of 2.7-Zr from EBSD. (b) High magnification IPF+IQ of 2.7-Zr. (c) Optical microscopy image of 2.7-Zr to compare Dendritic Arm Spacing (DAS) with b). (d) Low magnification IPF+IQ of 1.1-Y + 1.4-Zr and (e) grain size distribution for the region scanned in (d). Colors in (a) and (b) correspond to crystal orientations parallel to the out-of-plane direction as per the legend in the inset.

The low magnification Image in Figure 2a indicates a dendritic microstructure with relatively large grain size (> 600  $\mu$ m), which may impart improved creep resistant properties to the material, as seen in Ni-based superalloys<sup>49,50</sup>. The high magnification image in Figure 2b shows the second phase surrounding the Ni-matrix as expected from the eutectic present in the phase diagram<sup>33</sup>. The dendritic arm spacing (DAS) was obtained for these samples using the direct measurement method<sup>51</sup> where the average of at least 10 measurements was taken with error range calculated using the average absolute deviation. In Figure 2b, the DAS was measured to be  $8.0 \pm 0.7 \,\mu$ m, which was similar to that obtained from optical microscopy, i.e.,  $8 \pm 2 \,\mu$ m as seen in Figure 2c. Given that these measurements were obtained at different locations within the sample, the similarity between the two measurements is an indication of the homogeneity of the microstructure. In order to evaluate the grain size of Ni-Y-Zr alloys, the EBSD scans were performed at low magnification, an example of which is shown in Figure 2d for 1.1-Y + 1.4-Z with a scan area of 2456 x 2508  $\mu$ m<sup>2</sup>, showing a grain size between 1 and 2 millimeters with an area average of about 1.3 mm (Figure 2e).

Microstructures for the other compositions of Ni-Zr and Ni-Y shown in Table 1 were similar to those shown in Figure 2a with the DAS varying with compositions as shown in Figure 2. Moreover, the Ni-Y-Zr ternary samples also showed similar microstructure with a eutectic phase surrounding the matrix.

The comparison of the DAS of various Ni-Y-Zr alloys is shown in Figure 3b and indicates that the DAS decreased as the amount of alloying elements increased, due to the increase in the amount of eutectic phase, as expected<sup>33</sup>, in agreement with the findings for Ni-Zr binary alloys by Maity et al.<sup>16</sup> and J. M. Park et al.<sup>52</sup>, leading to the refinement of the microstructure. In the case of ternary Ni-Zr-Al alloys investigated by Maity et al.<sup>16</sup>, the DAS first increased with an increase in Al content and then decreased, in contrast to the gradual decrease seen in the Ni-Y-Zr alloys studied here (see Figure 3). This was due to

the fact that Al was added to the pre-synthesized Ni-Zr alloys with eutectic composition, leading to Al dissolving preferentially in the dendritic  $\gamma$ -Ni phase (due to solubility differences of Al in  $\gamma$ -Ni and Ni<sub>5</sub>Zr phases). This likely led to an increase in volume % of the  $\gamma$ -Ni phase, thereby increasing the DAS with increase in Al, as opposed to the continuous increase in intermetallic phase for the Ni-Y-Zr alloys studied here.

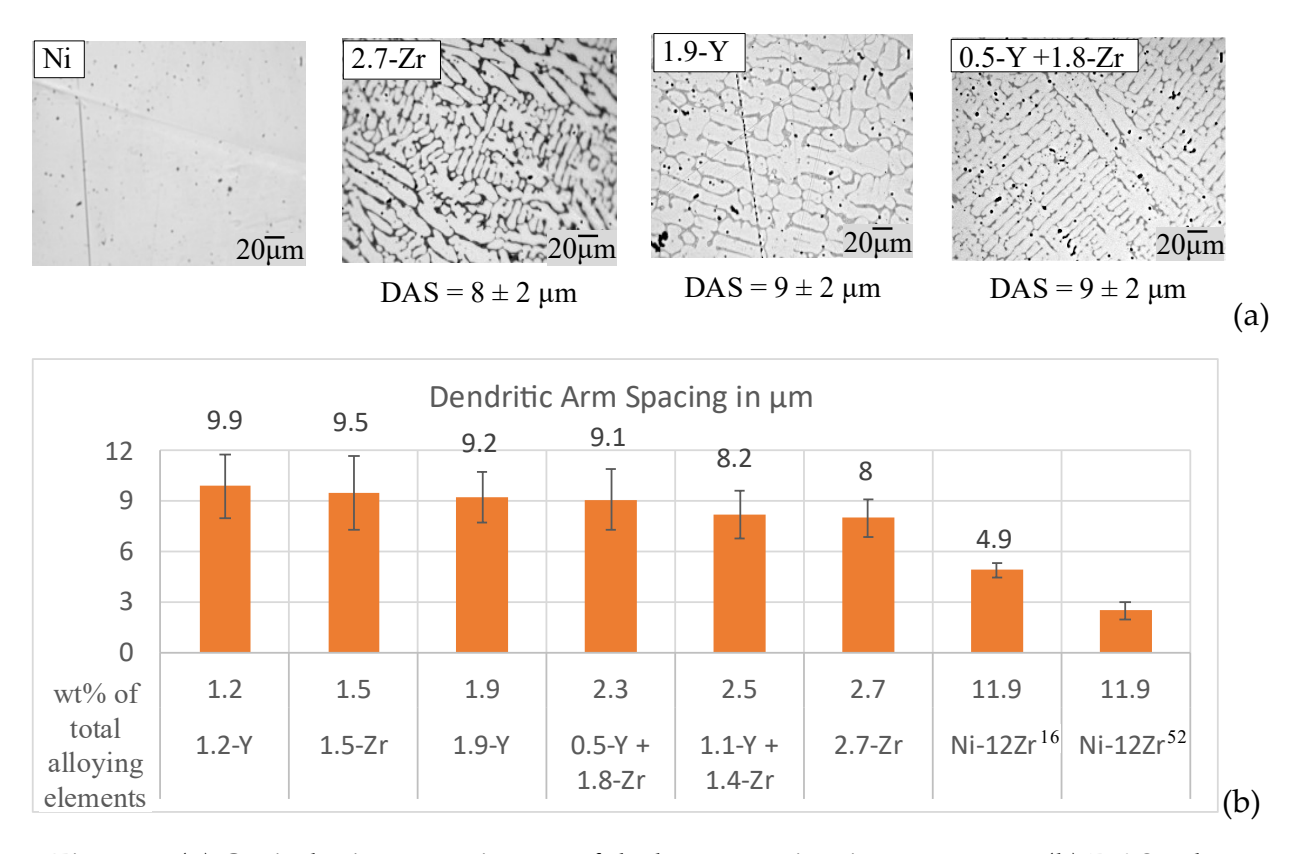


Figure 3. (a) Optical microscopy images of the hypoeutectic microstructures. (b) DAS values measured using EBSD and optical microscopy for the binary and ternary Ni-Y-Zr samples. Values for Ni-12Zr alloys reported in the literature 16,52 are shown for comparison.

The link between the DAS and the overall microstructure makes it a key microstructural parameter, in addition to the grain size. Another important length scale is the eutectic lamellar spacing, which is an integral part of the hierarchical microstructures of the material studied in this work. This length scale will be described next.

# 2.2 Characterization of eutectic phase

Backscatter electron imaging was performed on binary and ternary samples to study the distribution of intermetallic compounds (IMCs) and Ni-phase within the eutectic phase. Some typical results are shown in Figure 4 and Figure 5.

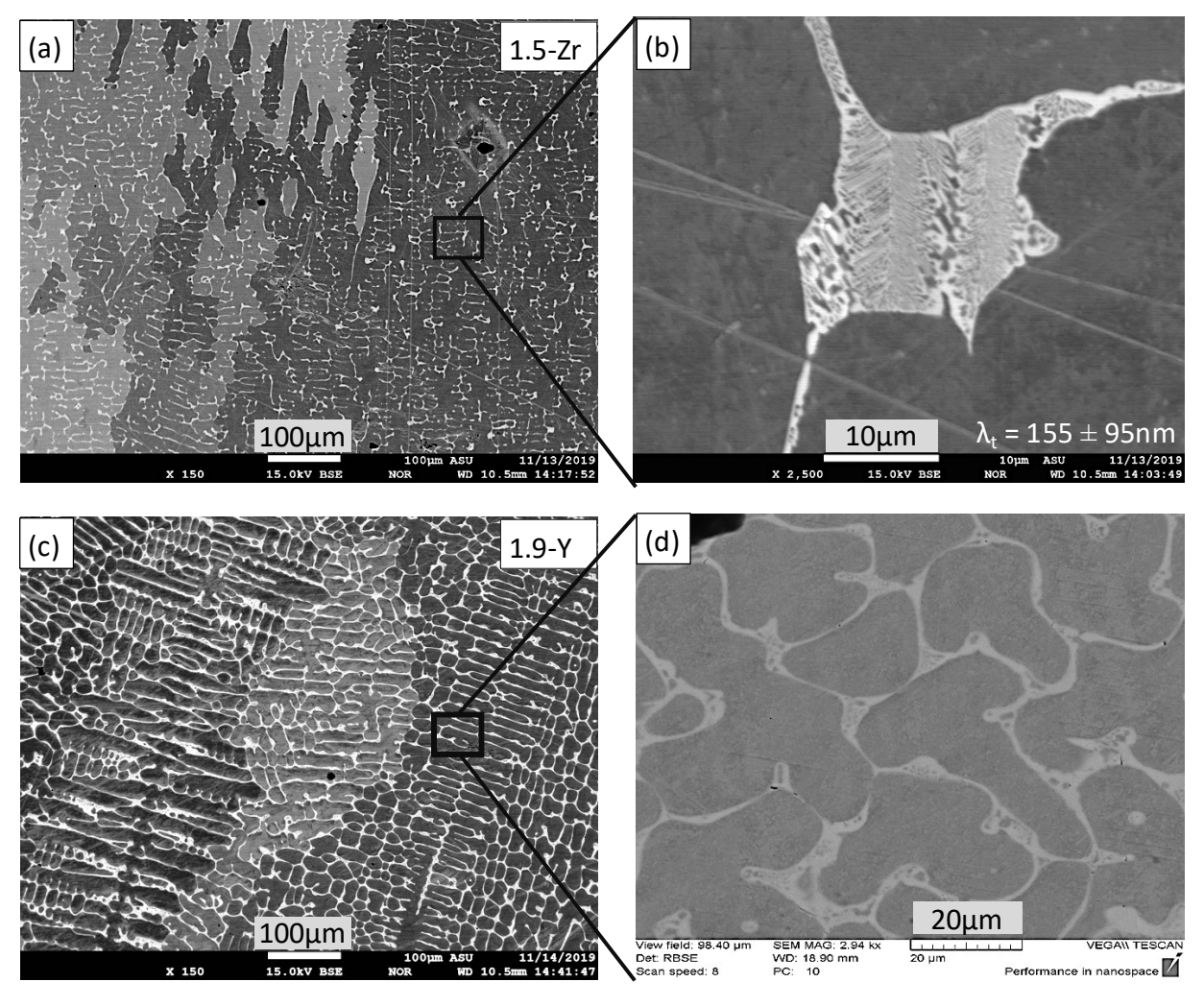


Figure 4. Backscatter electron images of binary alloys: (a) and (c) show the eutectic phase surrounding the Ni-matrix, (b) and (d) depict higher magnification images of the eutectic phase with Ni<sub>5</sub>Zr=brightest, Ni<sub>17</sub>Y<sub>2</sub> = light gray, and Ni = darkest.  $\lambda_t$  = average lamellar thickness.

For binary alloys, as seen in Figure 4, the BSE imaging verified the expected eutectic microstructure formed during the fast cooling of the samples in the tri-arc due to the water-cooled hearth. The different gray scales seen in Figure 4(a) and (c) indicate different grains, and eutectic region appears through most of the boundary between regions with

different gray scales, thereby decorating the grain boundaries. Additionally, given the difference in the atomic numbers of Ni, Zr, and Y (atomic numbers 28, 39 and 40, respectively), and the different compositions of the IMCs, there was enough Z-contrast from BSE imaging to reveal a proeutectic-dendritic Nickel-rich matrix formed due to constitutional supercooling surrounded by a eutectic phase of Ni and either of the two IMCs, Ni<sub>5</sub>Zr and Ni<sub>17</sub>Y<sub>2</sub>, as seen in Figure 4(b) and (d). Figure 5 shows images for the eutectic phase in ternary Ni-Y-Zr alloys.

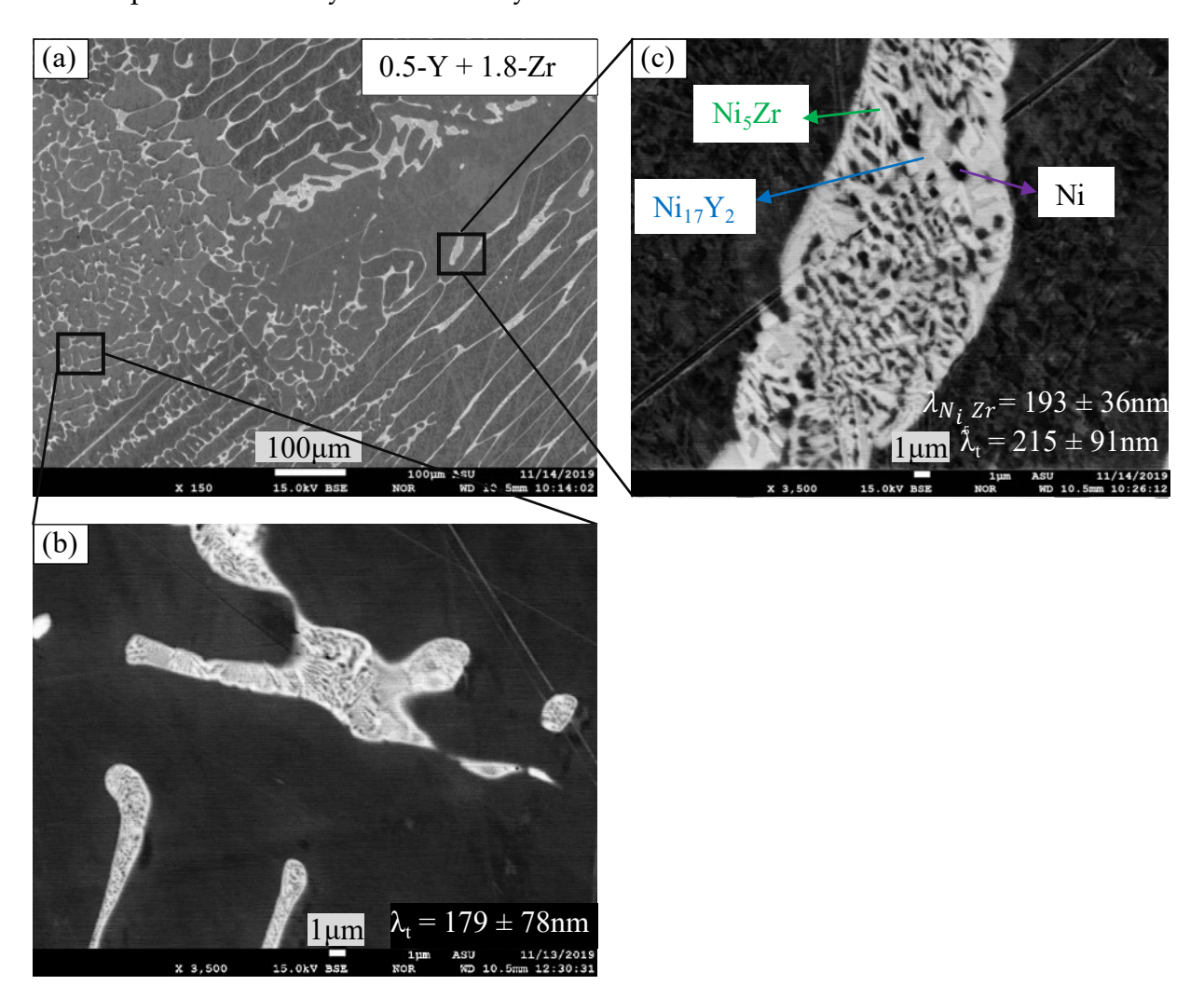


Figure 5. Backscatter electron images of a ternary Ni + 0.5wt%Y + 1.8wt%Zr alloy (a) eutectic phase surrounding the Ni-matrix, (b) and (c) higher magnification images showing the coexistence of  $Ni_5Zr$  and  $Ni_{17}Y_2$  in the eutectic phase with Ni ( $Ni_5Zr$ =brightest,  $Ni_{17}Y_2$  = light gray, Ni = darkest.  $\lambda_t$  = average lamellar thickness and  $\lambda_{Ni_5Zr}$  is the spacing between  $Ni_5Zr$  regions.

The high magnification images in Figure 5(b) and (c) depict the eutectic phase microstructure for Ni-Y-Zr alloys. As expected, the eutectic phase in the ternary alloys is a mixture of Ni<sub>5</sub>Zr and Ni<sub>17</sub>Y<sub>2</sub> along with the Ni phase. Clear distinctions between the phases are observed in Figure 5(c) with Ni<sub>5</sub>Zr as the brightest, followed by Ni<sub>17</sub>Y<sub>2</sub>, with Ni being the darkest. Thus, the eutectic structure had a semi-regular structure<sup>53</sup> with the Ni eutectic phase surrounded by the intermetallic phases, rather than the conventional lamellar structure. The average lamellar spacing ( $\lambda_t$ ) for binary and ternary specimens was, thus, measured as the width of the Ni-eutectic phase by taking at least 10 measurements with the error range calculated as the average absolute deviation. The  $\lambda_t$ values were found to be in the range of 150 to 300 nm for the samples, which is similar to that found by Park et al.<sup>52</sup> and Maity et al.<sup>14,16</sup> in their Ni-Zr alloys. In the case of ternary alloys, the co-existence of IMCs with Ni in the eutectic region, as seen in Figure 5(c) introduced yet another length scale that was termed  $\lambda_{Ni_5Zr}$  for the chains of Ni<sub>5</sub>Zr closely connected to eutectic-Ni and Ni<sub>17</sub>Y<sub>2</sub>, measured as 190 ± 40 nm for Ni + 0.5wt%Y + 1.8wt%Zr. Since  $\lambda_{Ni_5Zr}$  was in the same range as  $\lambda_t$ , the latter was considered the dominant length scale for ternary eutectic phases.

The BSE images also helped evaluating the area fractions of the two phases, dendritic and eutectic, present in the alloys, as shown in Figure 6. The area percentage was calculated using 2 to 3 images at 50x and 150x magnifications for each alloy and evaluating thresholds using ImageJ software to average at least 4 values for area fraction.

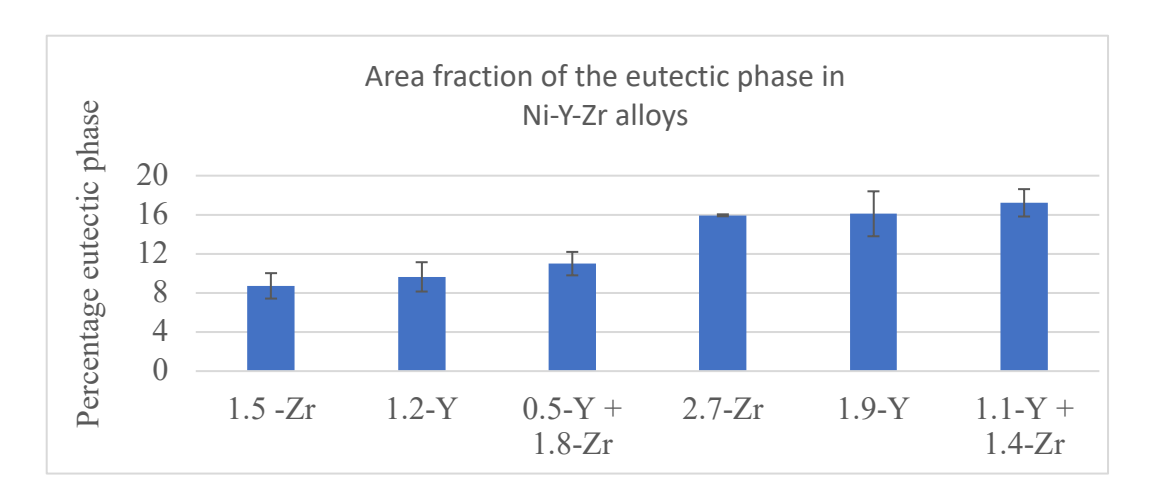


Figure 6. Comparison of the percentages of the eutectic vs. dendritic phases in Ni-Y-Zr alloys.

Figure 6 shows that samples 1.5-Zr, 1.2-Y, 0.5-Y+1.8-Zr had similar area percentages of the eutectic phase. Similarly, 2.7-Zr, 1.9-Y and 1.1-Y+1.4-Zr had the same area fractions of the two phases within the experimental scatter. Additionally, in the case of binary alloys, the eutectic area percentages were found comparable with values calculated using the phase diagrams<sup>33</sup>. Given the fact that Ni<sub>17</sub>Y<sub>2</sub> has higher Ni as compared Ni<sub>5</sub>Zr, lower wt% of Y displayed similar amount of eutectic phase as alloys with comparatively higher percentages of Zr. Moreover, this percentage plays a major role in the mechanical properties of the alloys due to the length scales involved.

The WDX measurements, which are shown in Figure S2 of the supplemental information, were performed with a probe diameter ~ 1  $\mu$ m, which was larger than the eutectic length scales. Hence, measurements for the eutectic phases corresponded to average compositions. It was found that the Ni-rich matrix had a maximum concentration of Zr below 0.6 wt% and no presence of Y for all alloys studied here, in agreement with the reported solubility limits of individual elements in Ni at room temperature, i.e., ~ 0.93 wt% for Zr and zero solubility (or negligible) for Y<sup>16,54</sup>. The eutectic phase had an average concentration of Zr in between the two extremes of Ni and Ni<sub>5</sub>Zr and Y in between Ni and Ni<sub>17</sub>Y<sub>2</sub>, indicating the presence of both eutectic-Ni and eutectic-intermetallic phases. In hypereutectic samples the matrix phase was rich in Zr and Y for Ni-Zr and Ni-Y

samples, respectively, as expected since the matrix should be made of the intermetallic compounds in these cases, with the percentages in or close to the range of the corresponding IMCs. These results confirmed the BSE observations: a microstructure fully consistent with the phase diagrams.<sup>33,50</sup> The next step was directed towards exploring mechanical behavior and microstructure stability, as described next.

# 2.3 Mechanical behavior and microstructure stability

## 2.3.1 Hardness Testing

Vickers hardness testing, the results of which are shown in Figure 7, revealed a significant hardness increase in the alloyed samples as compared to a reference pure nickel specimen that was arc-melted under the same conditions.

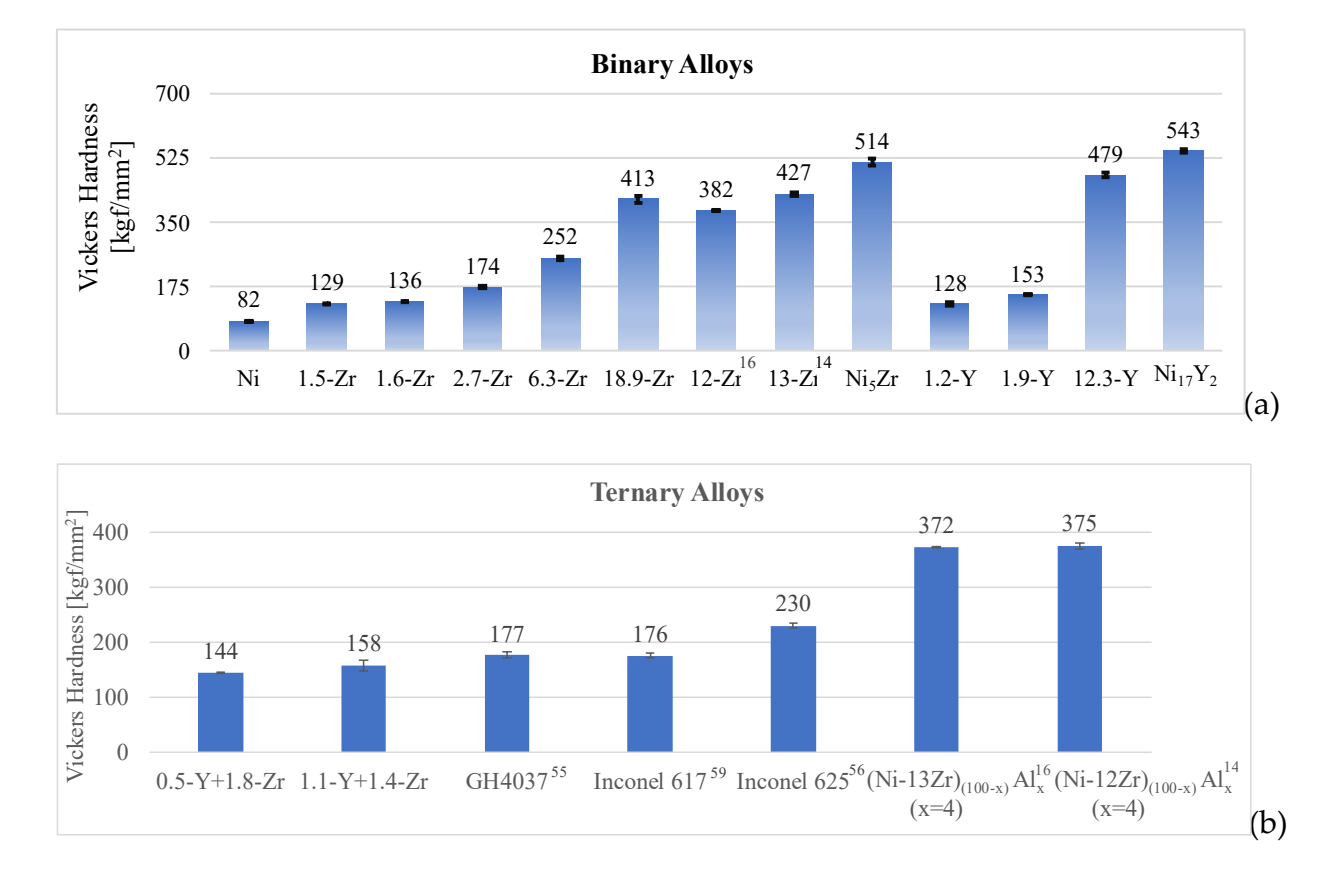


Figure 7.Vickers hardness as a function of composition for (a) binary and (b) ternary Ni alloys in comparison with Ni-based alloys<sup>14,16,55,56,59</sup>.

Note from the results in Figure 7 that the hardness increased with the increase in the percentage of alloying elements, as should be expected, given the corresponding increase in area percentage of the harder IMCs, as seen in Figure 6.

In order to compare the effect of alloying elements on mechanical properties of Ni alloys and superalloys more efficiently, we introduce a control parameter of hardness increase per wt% of solute added to pure Ni, calculated by dividing the increase in hardness of the alloys with respect to pure Ni with the total wt% of alloying elements present. Table 2 shows that where the total percent of alloying elements added to Ni-Y-Z alloys is ~2 to 3 wt%, those in Ni superalloys are ~40wt%. This represents the effectiveness of Ni-Y-Zr alloys in reaching mechanical properties comparable with Ni superalloys with only small addition of alloying elements. Thus, Ni-Y-Zr alloys show promising results with significant reduction in cost and complexity.

*Table 2. Comparison of Hardness per wt% solute within Ni alloys* <sup>14,16,55,56,59</sup>.

Alloys	Total alloying	Hardness	Hardness increase per
Anoys	elements (wt%)	(kgf/mm²)	wt% solute added
0.5-Y + 1.8-Zr	2.3	144	27.0
1.1-Y + 1.4-Zr	2.5	158	30.4
GH4037 55	23.63 to 38.24	177	4.0 to 2.5
Inconel 617 <sup>59</sup>	45.57	176	2.1
Inconel 625 <sup>56</sup>	38.72	230	3.8
(Ni-13Zr)96 Al4 16	14.6	375	20.1
(Ni-12Zr)96 Al4 <sup>14</sup>	13.49	372	21.5

The stability of the resulting microstructures is key for practical applications and is examined next.

### 2.3.2 Heat treatment

The heat-treated samples, cooled by water-quenching, were studied using EBSD to evaluate their microstructural stability. Measurements of grain sizes before and after heat treatments are shown in Figure 8 for the 1.1-Y+1.4-Zr alloy.

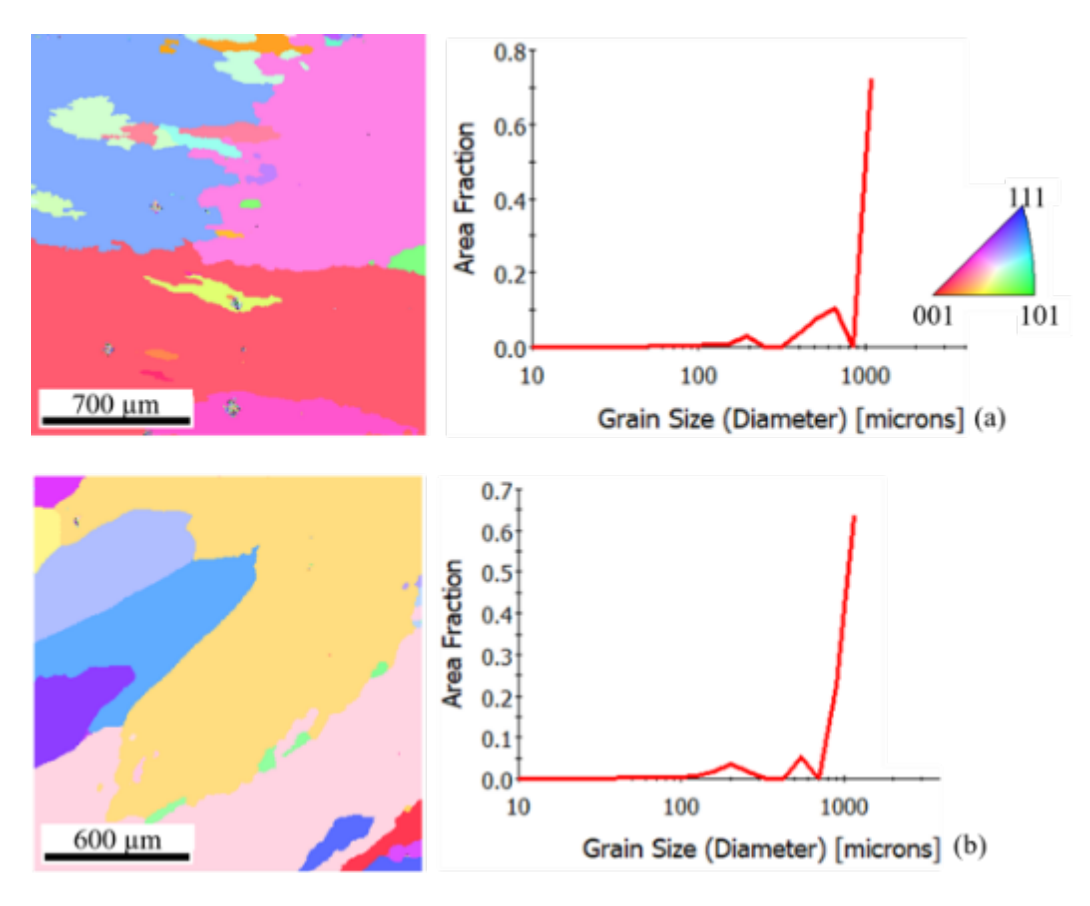


Figure 8. EBSD Imaging of 1.1-Y + 1.4-Zr at 112x magnification to evaluate the grain size of the sample (a) before heat treatment with a scan area of 1866 x 1902  $\mu$ m<sup>2</sup> (b) after heat treatment followed by water-quenching with a scan area of 1608 x 1642  $\mu$ m<sup>2</sup>.

The area average grain sizes recorded for 1.1-Y + 1.4-Zr both before and after heat treatment were 1035  $\mu$ m and 934  $\mu$ m, respectively, as shown in Figure 8, thereby indicating stable grains in case of Ni-Y-Zr alloys. To further explore the stability of the microstructure at smaller length scales, BSE imaging was performed at higher magnification as shown in Figure 9 to study the heat treatment impact on dendritic length scales. Area fractions of the eutectic and matrix phases were also calculated from these images as shown in Figure 10.

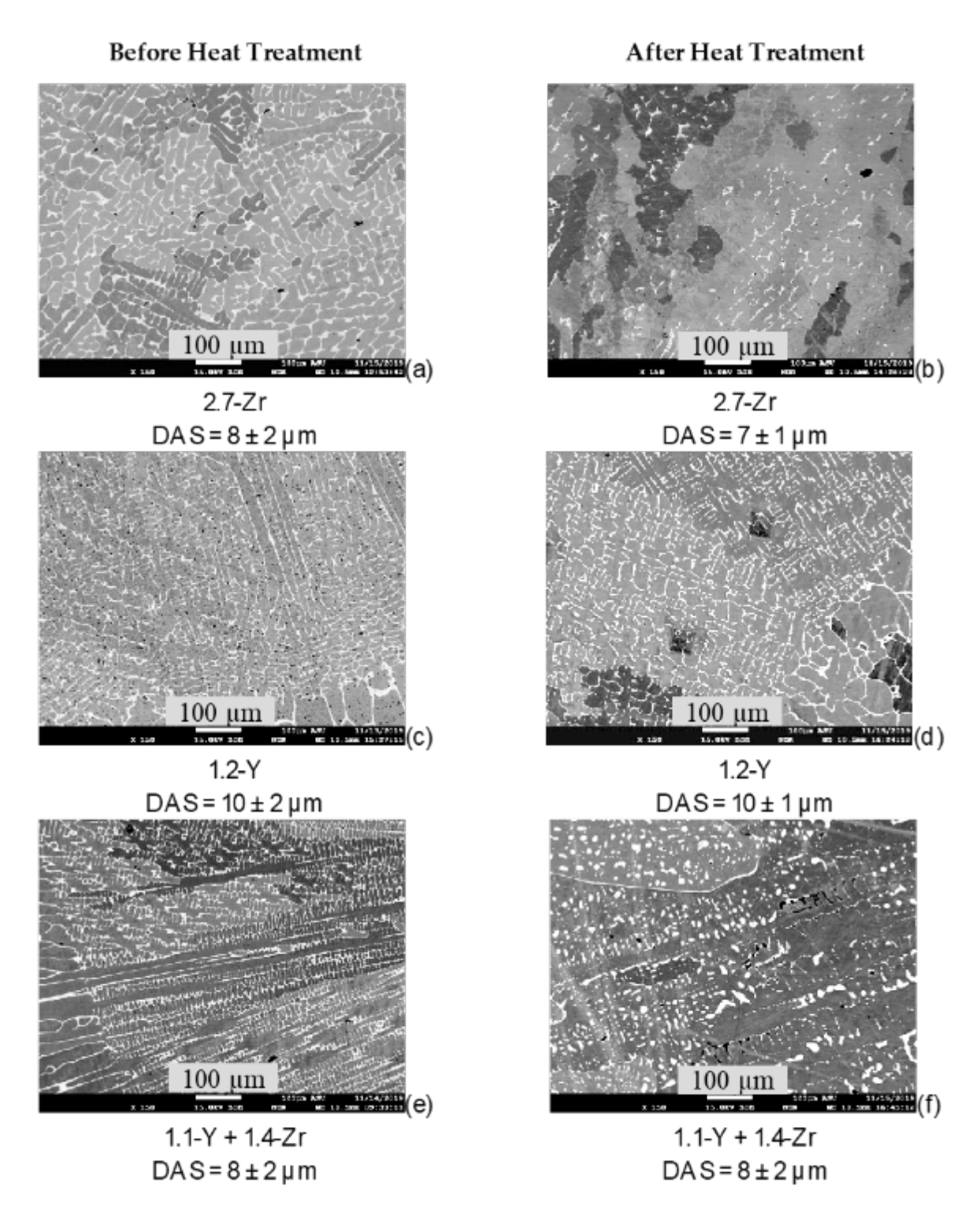


Figure 9. (a)-(f) BSE images of Ni-Y-Zr samples before and after the heat treatment and resulting DAS value.

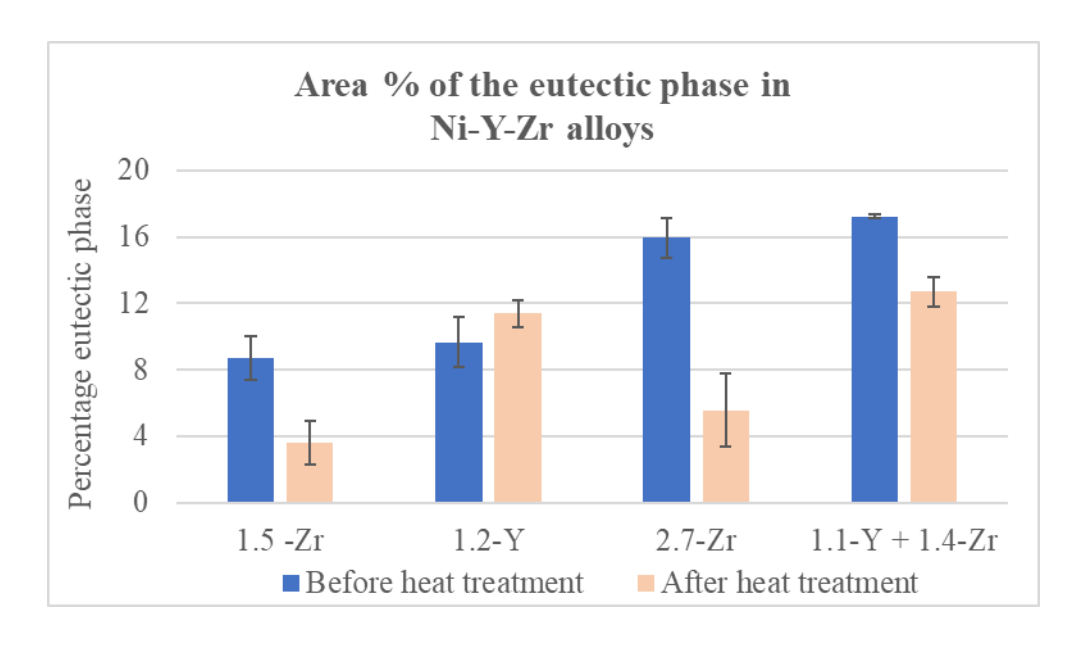


Figure 10. Comparison of the percentages of eutectic phases before and after the heat treatment.

As seen in Figure 9 and Figure 10, the amount of eutectic phase in Ni-Zr alloys decreased significantly (by ~60%) due to the increased solubility of Zr in Ni at higher temperatures, whereas the eutectic phase in the Ni-Y samples remained essentially the same (within the scatter band) even after heat treatment at 1100 °C as Y has ~ zero solubility in Ni<sup>33</sup>. In the case of Ni-Zr-Y, a combined effect was observed where the amount decreased only by ~26%. However, the DAS did not show a significant change in either of the binary or ternary alloys. A WDX analysis was performed to quantify any composition changes in each phase before and after the heat treatment as shown in Figure 11.

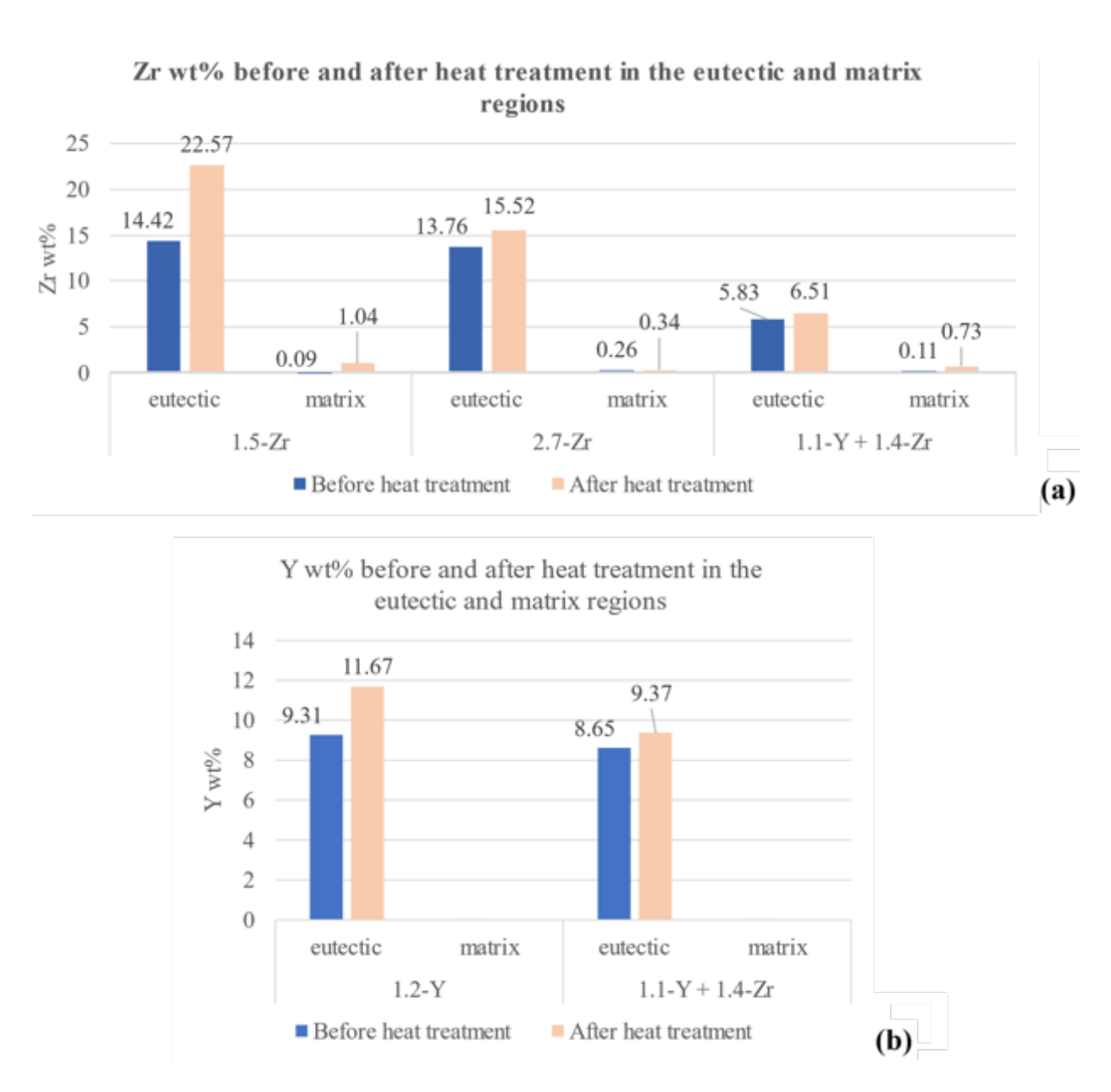


Figure 11. Results from WDX analysis. (a) Zr and (b) Y content in the eutectic phase and dendritic Ni-rich matrix before and after heat treatment.

The percentage increase of the Zr in the matrix (about 30% for 2.7-Zr) is higher than in the eutectic phase (about 12% in 2.7-Zr) owing to the increased solid solubility of Zr in Ni at high temperatures. No such increase is observed in the case of Y due to near zero solubility of Y in Ni. However, there is also an increase in alloying elements, both Y and Zr, observed in the case of the eutectic phase. This increase was further investigated using BSE imaging of the eutectic phase at higher magnification that showed coarsening of both

IMCs (Ni $_5$ Zr and Ni $_1$ 7Y $_2$ ) as depicted in Figure 12. Hence, the increase in the wt% of Y and Zr in the eutectic is likely due to an increase on the area fraction of the IMCs in the region analyzed with WDX, as the coarsened IMCs could have sizes similar to the probe.

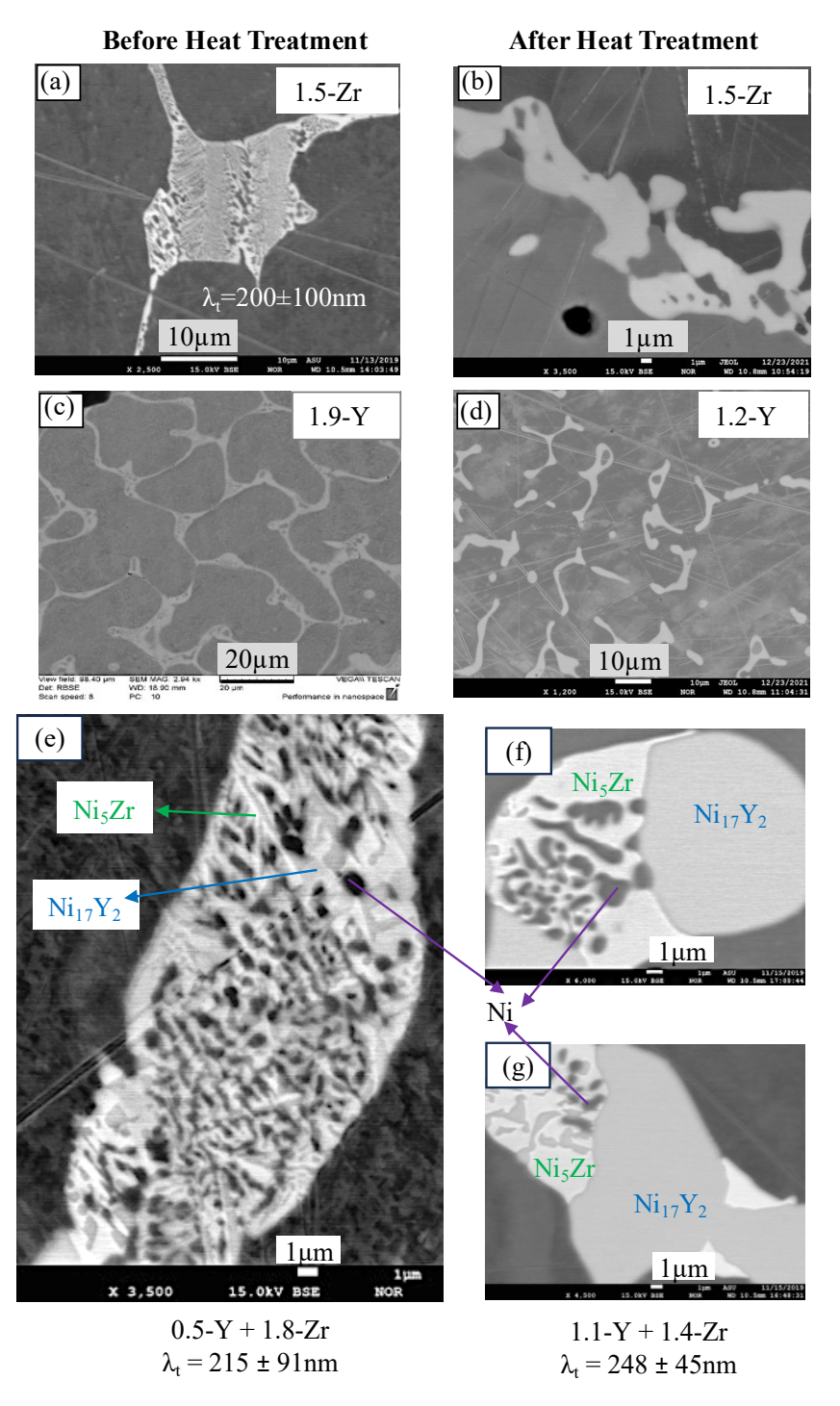


Figure 12. High magnification BSE images of the eutectic phase of Ni-Zr, Ni-Y and Ni-Y-Zr (a), (c), (e): before; (b), (d), (f), and (g): after heat treatment.

The  $\lambda_t$  of Ni-Y-Zr samples after the heat treatment remained in the range of 150 to 300 nm, despite the coarsening that was observed for both Ni<sub>5</sub>Zr and Ni<sub>17</sub>Y<sub>2</sub> IMCs, with Ni<sub>17</sub>Y<sub>2</sub> coarsened significantly more. To study the effect of this coarsening on the mechanical properties, Vickers hardness testing was performed on the heat-treated samples, with results shown in Figure 13.

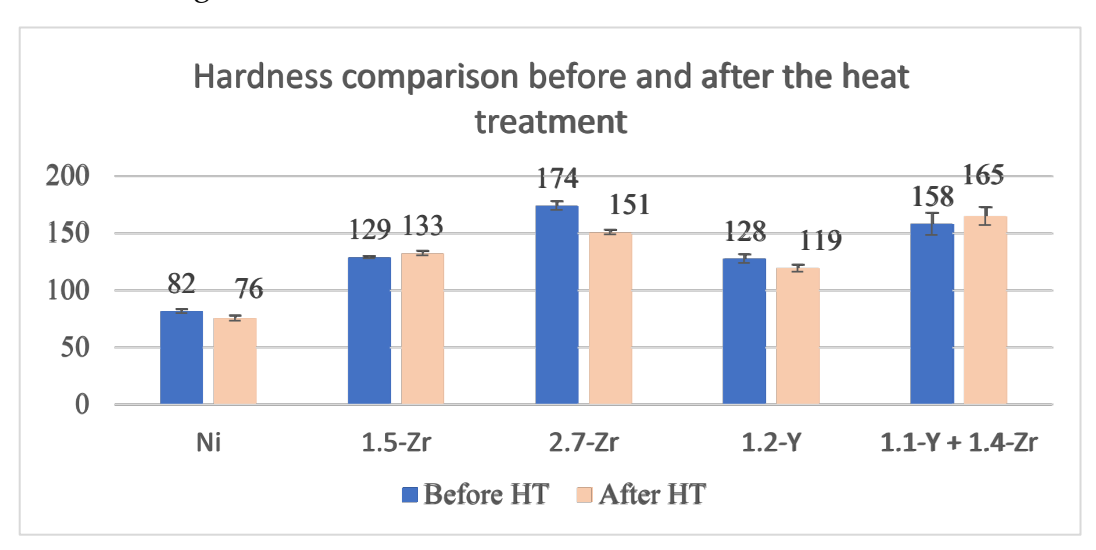


Figure 13. Vickers hardness of Ni-Zr-Y samples before and after heat treatment.

It was observed that the hardness of the samples after heat treatment stayed within the error range despite the decrease in the area fraction of the eutectic phase and its discontinuity ("broken" eutectic phase) in case of Ni-Zr and Ni-Y-Zr alloys. This would be further discussed in detail in section 3.2.

# 2.3.3 Compression Testing

For uniaxial compression testing at room temperature and 600°C, the compositions used to investigate the stress-strain response were chosen based on similar eutectic area fractions (refer to Figure 6) to provide an effective comparison between binary and ternary alloys, as shown in Figure 14, Figure 15 and Table 3.

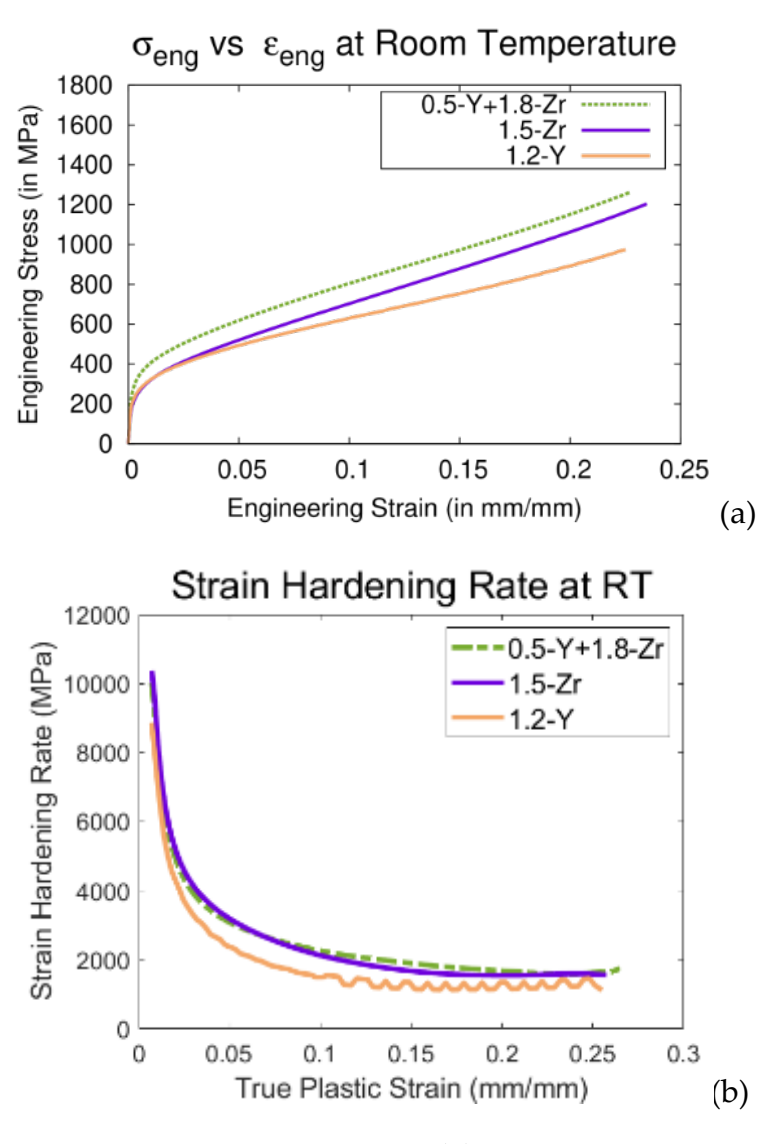


Figure 14. (a) Engineering Stress-strain curves and (b) corresponding strain hardening rates for a strain rate of 0.0048 min<sup>-1</sup> ( $8x10^{-5}$  s<sup>-1</sup>) for 1.5-Zr, 1.2-Y, and 0.5-Y+ 1.8-Zr at RT to ~20% strain.

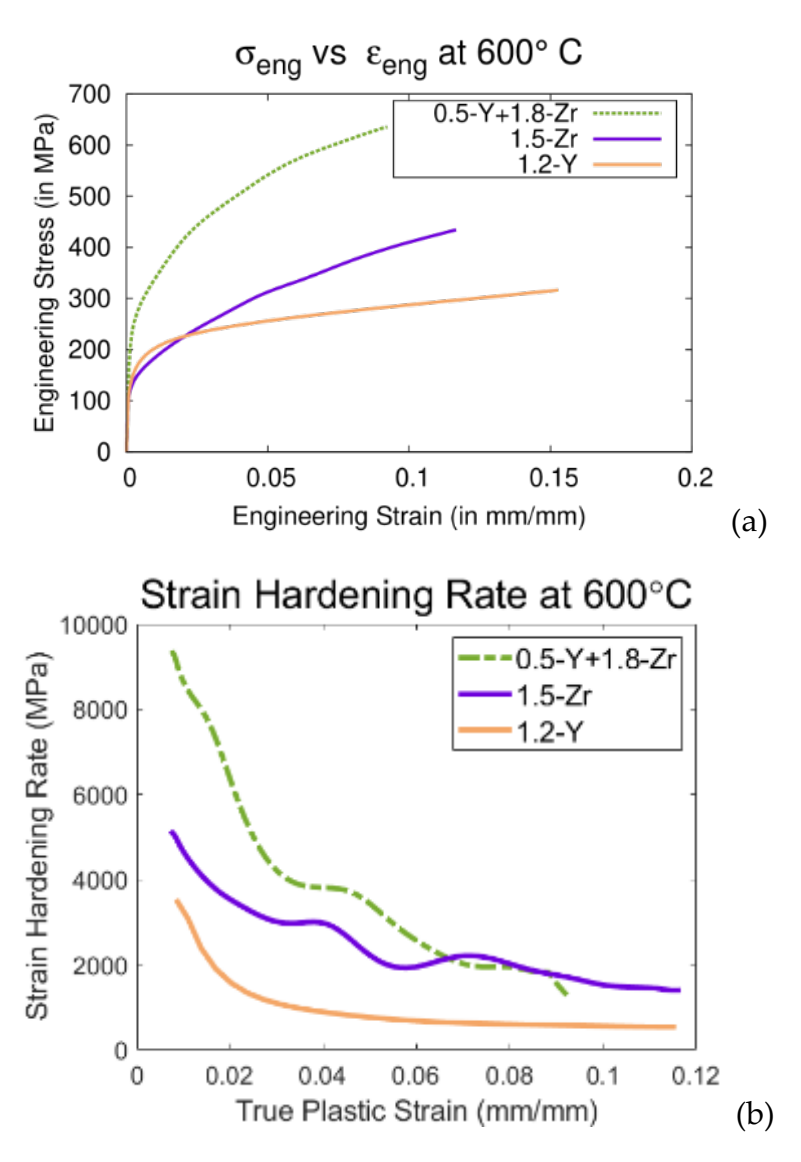


Figure 15. (a) Engineering Stress-strain curves and (b) corresponding strain hardening rates for a strain rate of  $0.0048 \text{ min}^{-1} (8x10^{-5} \text{ s}^{-1})$  for 1.5-Zr, 1.2-Y, and 0.5-Y+ 1.8-Zr at  $600 \,^{\circ}\text{C}$  to  $10\% \,^{\circ}$  strain.

Figure 14 and Figure 15 display the stress-strain behavior of 1.5-Zr, 1.2-Y and 0.5-Y+1.8-Zr alloys tested under a strain rate of  $0.0048 \text{ mm/mm/min} (8x10^{-5} \text{ s}^{-1})$ . All compositions, at both test temperatures (RT and  $600^{\circ}$ C), exhibited work hardening, and in between the binary alloys, 1.5-Zr and 1.2-Y, the former has the lowest yield strength but the highest hardening rate. Moreover, as seen in Figure 14, Figure 15 and Table 3, the ternary alloy (0.5-Y+1.8-Zr) shows a synergistic effect: yield strength that is higher than either binary, but with a hardening rate similar to that of Ni-Zr alloy.

Table 3. Mechanical properties of the Ni-Y-Zr alloys and intermetallic compounds in comparison to Ni-based superalloys.

Samples	Yield Str	Hardness (kgf/mm²)	
Jumples	RT	600°C	Transmit y
1.5-Zr	224	140	129 ± 1
1.2-Y	245	161	127 ± 4
0.5-Y+ 1.8-Zr	318	268	170 ± 10
Inconel 617	35057	216 <sup>58</sup>	$176 \pm 5^{59}$
Inconel 625	$498^{60}$	$362^{61}$	$230 \pm 5^{56}$

The next section will focus on a discussion of these results and their relation to structure and composition of the Ni-Y-Zr alloys.

#### 3. Discussion

### 3.1 Hardness measurements

The samples with 2.7 wt% Zr and 1.1 wt% Y + 1.4wt% Zr had a hardness of about two times that of the pure nickel reference sample, as shown in Figure 7. In addition, the value of hardness for these samples with small percentages of alloying elements is actually comparable to that obtained in existing Ni-based alloys, which are known for their excellent strength and high temperature creep resistance<sup>28</sup>. Comparing the hardness values of samples with ultrafine eutectic samples of Ni-Zr-Al, the Ni-Y-Zr alloy studied here displayed a hardness of about half of that of Ni-Zr-Al alloys, but with the amount of alloying elements in the former being less than half of those used for the latter<sup>14,16</sup>. Higher hardness of the Ni-Zr-Al alloys studied by Maity et al<sup>14</sup> are to be expected since they involved eutectic or near-eutectic<sup>16</sup> compositions of Ni-Zr, leading to extremely high fraction of eutectic phase (between 80% and 100% eutectic phase) as compared to Ni-Y-

Zr (16 – 20 % fraction of eutectic phase). However, the alloys studied by Maity et al <sup>14</sup> showed a decrease in hardness with Al additions due to an increase in the DAS, unlike the ternary alloys studied here for which there was a refinement of microstructure in terms of reductions for both DAS and  $\lambda_t$ . This suggests that Y additions are more beneficial than Al additions to improve the strength of Ni-Zr alloys.

Therefore, the above two trends in hardness indicate the improvement of properties of Ni-alloys by the addition of Zr and Y through solid solution strengthening due to some solubility of Zr in Ni and second phase formation, with Ni<sub>17</sub>Y<sub>2</sub> and Ni<sub>5</sub>Zr IMCs present in the eutectic phase, as well as potential precipitates in the Ni-rich matrix.

Effects of heat treatment on microstructure and mechanical properties will be discussed next.

#### 3.2 Heat treatments

The Ni-Y-Zr alloys exhibited stable grain size, an example of which is shown in Figure 2. This can be explained using results from Figure 4, which shows that grain boundaries are decorated by the eutectic phase. Thus, the IMCs apply a retarding/drag force on the movement of the boundaries at high temperature, imparting stability to the grains. Similar effects of intermetallic compounds were observed in case of other length scales, i.e., DAS and  $\lambda_t$ , leading to the stability of the microstructure at high temperatures.

The coarsening of the IMCs shown in Figure 12 was further explored by performing EBSD measurements at higher resolutions (spot size = 87.3 nm, and probe current = 532 pA) to study the orientation relationship between the Ni and IMC phases as shown in Figure 16.

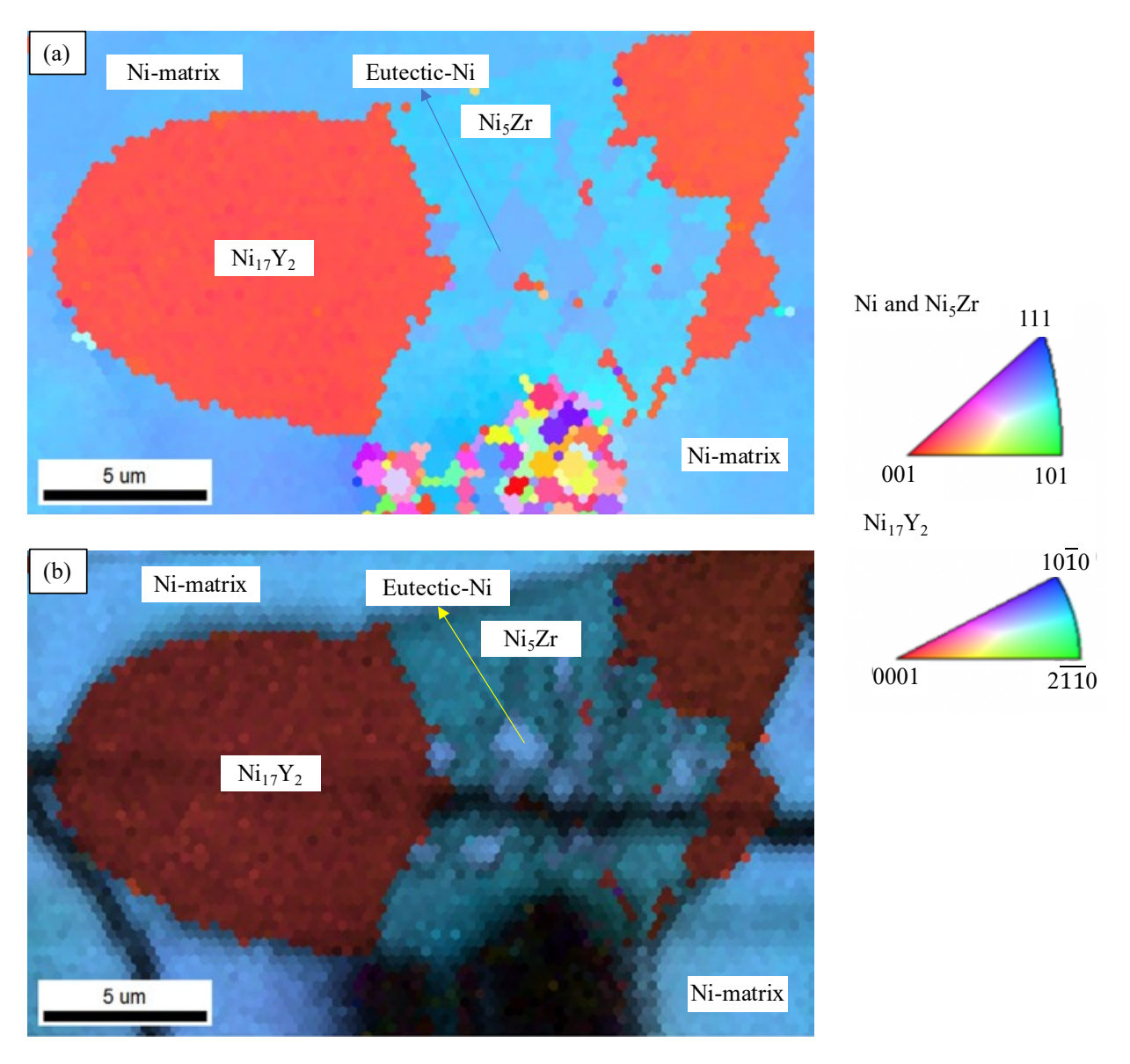


Figure 16. Results from EBSD measurements of the eutectic phase region shown in Figure 5b (a) shows the IPF map with the phases labelled, (b) IPF+IQ mapping for further distinction. Note that the colors in (a) and (b) correspond to crystal orientations parallel to the out-of-plane direction as per the legend in the inset, the dark lines seen in (b) are scratches introduced during polishing of the specimen, whereas the dark region toward the bottom corresponds to a Vickers indent used as a fiducial.

The EBSD analysis indicated that the misorientation between the Ni-rich phase and the Ni<sub>5</sub>Zr intermetallic corresponds to a rotation of 30° about the <111> axis that is common to the Ni and the Ni<sub>5</sub>Zr phases, both of which are FCC. This misorientation suggests that the (111) planes of both phases are parallel, with the <110> direction of Ni parallel to the

<112> direction of Ni<sub>5</sub>Zr, which is consistent with the data found in literature<sup>52</sup>. No such orientation relationship could be established in case of Ni and Ni<sub>17</sub>Y<sub>2</sub>, which along with the rounded interface between Ni<sub>17</sub>Y<sub>2</sub> and the Ni matrix, points to an incoherent interface between Ni<sub>17</sub>Y<sub>2</sub> with Ni. The lack of interfacial coherency, which is also consistent with the lattice mismatch<sup>30,31,33,45,46</sup> between the two phases, is likely a significant driver of the coarsening of the Y-bearing IMC. Similar coarsening effects have been reported in Ni superalloys<sup>62-64</sup>.

In the heat-treated samples, while the DAS and  $\lambda_t$  remained the same, the amount of eutectic decreased for Ni-Zr and Ni-Y-Zr alloys. Hence, one would expect the samples to show a decrease in hardness. However, the hardness of all the alloys before and after heat treatment remained the same within experimental scatter. Thus, one can argue based on the rule of mixtures, that the hardness of the matrix increased, most likely due to the solubility of Zr in the matrix. Another thing to point out from Figure 9 is that the heat treatment made the eutectic phase discontinuous, which means that the eutectic phase cannot be as effective as a reinforcement as it was in the untreated samples, also indicating that the matrix must be harder now. This was studied further assuming the overall hardness can be estimated through the rule of mixtures:

$$Hardness = v(eu)H(eu) + v(Ni_m)H(Ni_m)$$
 Eq. 1

where, v(eu)= area fraction of eutectic, H(eu)= hardness of the eutectic phase,  $v(Ni_m)$ = area fraction of Ni matrix and  $H(Ni_m)$  is the hardness of the Ni matrix. The above equation, for calculating the hardness of Ni-Zr alloys can then be deduced as:

$$H(Ni - Zr \ alloys) = v(eu)H(Ni_{eu} + Ni_5Zr) + v(Ni_m)H(Ni_m),$$
 Eq. 2

where,  $H(Ni_{eu} + Ni_5Zr)$  is the hardness of Ni in the eutectic phase and Ni<sub>5</sub>Zr IMC. Given the difference in the size of Ni in the matrix and the eutectic phase, the Hall-Petch

equation was used as given by Cordero et al. to evaluate a correlation between the hardness of Ni in the two phases. Furthermore, using the correlation and Eq 2, the following results were obtained as shown in Table 4.

*Table 4. Hardness of Ni matrix before and after heat treatment (HT).* 

Ni-Zr alloys	$H(Ni_m)$ in (kgf/mm <sup>2</sup> )		
	Before HT	After HT	
1.5-Zr	100	118	
2.7-Zr	126	131	

As inferred from the table above, the hardness of Ni in the matrix increases after heat treatment, thereby validating the above-established hypothesis. As seen in Figure 11, wt% Zr present in the matrix increases after heat treatment. Thus, the increase in hardness of the matrix post heat treatment could be attributed to solid solution strengthening. Additionally, the percentage increase of the hardness of the matrix for 1.5-Zr is 18%, whereas for 2.7-Zr is only 5.56%, in accordance with the significantly high increase in wt% Zr in matrix post heat treatment for 1.5-Zr as compared to 2.7Zr (refer Figure 11). This could be because 2.7-Zr is very close to the maximum solid-solubility limit of Zr (2.74 wt% Zr at eutectic temperature).

These solid-solubility effects are also likely to aid in work hardening during compression tests and will further be analyzed and discussed next.

### 3.3 Compression testing

The results of the compression tests on the binary and ternary alloys displayed a trend in work hardening and yield stresses of the alloys (refer in Figure 14, Figure 15 and Table 3) that was linked to their compositions. This trend was analyzed further based on the

interactions of the IMCs with the Ni-matrix. Comparing the two binary alloys, 1.5-Zr had a higher hardening rate and lower yield stress than 1.2-Y. While this in Ni-Y alloys can be attributed only due to the presence of the intermetallic phase, Ni<sub>17</sub>Y<sub>2</sub> (negligible solubility of Y in Ni)<sup>33</sup>, solid-solution strengthening also seems to play a role in the hardening rate of Ni-Zr alloys, as seen in Figure 14(a) since the work hardening rates for the 1.5-Zr is higher than for the 1.2-Y sample, at a similar area fraction of eutectic phase. Additionally, the heat treated Zr bearing samples had similar hardness as the untreated samples despite a significant reduction in the area fraction of eutectic phase, but similar trend of work hardening is also observed at high temperature compression tests (Figure 15a)).

The initial results indicate that the effect of intermetallic phases in Ni-Zr and Ni-Y alloys on yield strength and hardness is comparable given that they have similar amounts of dendritic/eutectic phases (refer to Figure 6). Thus, the higher hardening rates observed in the Zr-bearing alloys suggest the potential presence of dispersoids of Ni<sub>5</sub>Zr in the matrix, as is the case in precipitation hardened Ni-superalloys<sup>50,65</sup>. A quantification of the effect of solid-solution strengthening in 1.5-Zr alloy and its difference from experimental results might provide additional insight into the potential presence of precipitates.

It has been established that Zr has a substitutional solid-solution strengthening effect for the Ni-matrix<sup>66,67</sup>. Thus, the difference between the flow stress of the unalloyed metal vs a solid solution was evaluated using the following equation<sup>68</sup>:

$$(\Delta\sigma)_{ssh} = \sigma_{ss} - \sigma_0 = k_{ssh}c^a, Eq. 3$$

where,  $k_{ssh}$  is the solid solution hardening, c is the atomic fraction, and a=0.5 according to Friedel<sup>69</sup> and Fleischer<sup>67</sup> in their strong-pinning model where the solute atoms in the glide plane are considered as independent point obstacles pinning the dislocations, whereas a = 2/3 according to the Labusch's theory<sup>70</sup> that considers the statistical

distribution of the solute besides the effect of temperature within the weak-pinning model. The mechanisms described in Labusch's theory are considered the ones controlling the strength at most temperatures (T > 78K) and solute concentrations ( $c > 10^{-4}$ ) <sup>71,72</sup>. Thus, Wang et al. <sup>72</sup> recently proposed an improved model by incorporating the misfit factor into Labusch's model through the following equation to calculate solid solution strengthening:

$$(\Delta\sigma)_{ssh} = 3ZG\varepsilon^{\frac{4}{3}}c^{\frac{2}{3}}$$
 Eq. 4

where, Z =0.002 is a constant dependent on the solvent, and G is the shear modulus calculated using:

$$\bar{G} = K_G c + \bar{G}_0$$
 Eq. 5

 $\bar{G}=96~GPa$  and  $\bar{G}_0=99.3~GPa$  are the Voigt-Reuss-Hill (VRH) shear moduli of the solid solution model for 1.5wt%Zr and pure FCC Ni, respectively,  $K_G=-320.3~GPa$  is a linear correction coefficient,  $\varepsilon=3.2634$  is the misfit strain dependent on lattice and modulus misfit parameters, and c=0.01 is the atomic fraction of Zr in Ni. These values were either taken or calculated using the supplementary data provided by Wang et al<sup>72</sup>. Thus,  $(\Delta\sigma)_{ssh}$  is calculated to be ~ 130 MPa for 1.5wt%Zr. As seen from Figure 14(a), we can see that the difference in between the stresses for Ni-Y and Ni-Zr curve keeps increasing beyond 130 MPa. This suggests that the additional strengthening could be perhaps imparted by potential dispersoids in Ni-Zr alloys that are absent in Ni-Y alloys due to insolubility of Y in Ni<sup>33</sup>.

Additionally, research by Park et al.<sup>52</sup> and Maity et al.<sup>16</sup> shows that the Ni<sub>5</sub>Zr IMC plastically deforms with the Ni rich phase, thereby contributing to the strain-hardening. This co-deformation of matrix and eutectic also seems to occur for the ternary alloys, as suggested by images of the microstructure of samples deformed to fairly large strains (~40%) shown in Figure S3 of the supplemental information. However, in the increase in

flow stress of the ternary as compared to the Ni-Zr binary indicates that the Ni<sub>17</sub>Y<sub>2</sub> intermetallic is a very effective reinforcement when added to the eutectic phase. This can be compounded by the morphology of the eutectic phases as seen in Figure 16. If the eutectic in the Ni-Y alloys is cellular in nature, the deformation of the matrix phase might be fully contained inside the cells for the Ni-Y. Then, if one assumes that the Ni<sub>17</sub>Y<sub>2</sub> IMC is much stiffer plastically than the matrix (as suggested by hardness values in Figure 7) this will lead to slip in confined volumes within the matrix inside the cells that might saturate earlier, whereas deformation of the Ni-Zr phase (Ni<sub>5</sub>Zr), where the eutectic morphology is akin to channels that might form a bicontinous structure, might allow to spread the deformation across cells and that interaction across larger length scales might favor a higher hardening rate. This will further be explored in future work via 3-D characterization of the microstructures.

The synergistic combination of highest yield strength of the ternary alloy (0.5-Y+ 1.8-Zr) as compared to both 1.5-Zr and 1.2-Y with a hardening rate similar to that of Ni-Zr alloy can be explained by inspecting the elastic and plastic regimes of strains. At small strains, this synergy could be explained through combined effect of the two IMCs (Figure 4(f)), and the refinement of the microstructure (smaller DAS, as shown in Figure 3), leading to a higher yield strength. However, in the plastic regime, additional effects of the solid solution strengthening, along with potential dispersoid strengthening as evaluated through Eq. 4, could be the dominating factors providing resistance to slip. Lastly, another factor to note is that the fraction of the eutectic phase in the ternary, as seen in Figure 6, although in the error range, is still slightly higher than the two binary alloys. While this might contribute to the observed effects, it is unlikely to play a major role due to the small differences.

The results of the compression tests at 600 °C show quite clearly that the effectiveness of the Ni<sub>17</sub>Y<sub>2</sub> intermetallic phase as a reinforcement when added to the eutectic phase

improves significantly at high temperatures, leading to higher yield strengths and hardening rates as compared to Ni-Zr and Ni-Y alloys. This is most likely a result of its hexagonal structure, leading to more constraints on its plastic deformation as compared to the Ni<sub>5</sub>Zr cubic phase. Furthermore, the coarsening of Ni<sub>17</sub>Y<sub>2</sub> observed in the heat treated specimens, which was more pronounced than that for the Ni<sub>5</sub>Zr phase, is likely increasing this effect, since the larger size of this phase would lead to it acting as a more effective constraint to the deformation of the other phases inside the eutectic. At the same time, some dissolution of Ni<sub>5</sub>Zr is also to be expected, due to the increased solid solubility of Zr in the Ni-rich matrix. This, in turn, will increase the solid solution hardening of the matrix itself, which must be a factor that contributed to the higher hardening rates observed in the Ni-Zr binary alloys at 600 °C as compared to the Ni-Y binary alloy, since the solubility of Y in Ni is essentially zero.

The stress-strain behavior of the ternary alloy at high temperatures can be compared and contrasted with the behavior of the solution-strenthened nickel-based superalloys, in particular, Inconel 617 and Inconel 625 have been chosen here as typical examples, since the alloys produced from the melt in this work have not been heat treated to have extended precipitation in the matrix. As shown in Table 3, the room temperature and 600 °C yield strength of the ternary alloys studied in this work are fairly simialr to those of Inconel 617, and about 63 and 74% of the yield strength of Inconel 625 at room temperature and 600 °C, respectively, showing that the ternary alloys can reach mechanical properties well in the range of those obtained in highly optimized Ni-based superalloys. The solid solubility of Zr in the matrix is likely to play an important role on the more pronounced hardening rate observed at elevated temperatures in the alloys containing Zr, while the presence of the eutectic phase might be akin to the strengthening effects produced by carbides that can precipitate at the grain boundaries of solution-strengthened alloys such as Inconel 61773. The results indicate that the ternary alloys have

significant potential for enhanced mechanical behavior at high temperatures, due to the combination of solid solution hardening and strengthening from the dual  $Ni_5Zr/Ni_{17}Y_2$  eutectic phases.

#### **Conclusions**

In this work, we analyzed the microstructure of Ni-Y-Zr alloys, both binary and ternary, at low percentages of alloying elements to explore its impact on thermo-mechanical behavior. The ternary system of Ni-Y-Zr alloys at the compositions studied here showed a clear hierarchical microstructure defined through three major length scales, the grain size at the macroscale (~1 mm), the dendritic arm spacing (DAS) in the Ni-matrix at the microscale (~10  $\mu$ m) and the eutectic lamellar spacing ( $\lambda_t$ ) at the nanoscale (~200-300 nm). Where  $\lambda_t$  and DAS length scales were deemed to have a major impact on microstructural stability and mechanical properties like hardness and strain hardening, the large grain sizes are expected to provide increased creep resistance to Ni-Y-Zr alloys as seen in Ni superalloys<sup>49,50</sup>.

Furthermore, the synergistic interactions of the Ni<sub>5</sub>Zr and Ni<sub>17</sub>Y<sub>2</sub> phases on different length scales and their impact on the thermo-mechanical properties were further explored. It was seen that even at temperatures as high as 1100°C, the microstructure remained stable in terms of length scales as no appreciable change was observed in grain size, DAS and λ<sub>t</sub>. However, the amount of eutectic phase decreased significantly in case of Ni-Zr and Ni-Y-Zr alloys due to solubility of Zr in Ni, with no considerable change in Ni-Y alloys due to insolubility of Y. Additionally, coarsening of the phases was also observed similar to that seen in Ni-superalloys<sup>62-64</sup>. The hardness of heat-treated samples did not change significantly compared to that of the untreated specimens, which suggests that the coarsening of the IMCs within the eutectic did not have a strong impact on mechanical properties, while the increased solubility of Zr in the Ni-rich matrix leads to

an improved solid solution hardening that compensates for a decrease in the volume fraction of eutectic phase.

In case of uniaxial compression tests at room and high temperatures, the highest yield strength was found for the ternary alloys whereas the Ni-Zr and Ni-Y-Zr allows had higher hardening rates than Ni-Y alloys, which reached saturation at much lower strains. This is likely due to solid solution hardening and the potential present of matrix dispersoids in Ni-Zr alloys. These results also show than the Ni<sub>17</sub>Y<sub>2</sub> IMC is a very effective reinforcement when combined with Ni<sub>5</sub>Zr within the eutectic phase of the ternary alloys with its effectiveness increasing with temperature, most likely as a result of limited plasticity due to its hexagonal crystal structure. The results suggest that Ni-Y-Zr alloys hold significant promise as potential structural materials with two-fold increase in hardness as compared to Nickel with only a few wt% addition of alloying elements, stable microstructures at high temperatures and yield strength comparable to Ni superalloys.

### Acknowledgements

The work by S.S., S.S., S.M., K.S. and P.P. was supported by the US National Science Foundation, Division of Materials Research under grant DMR-1810431. X-ray diffraction measurements were performed at Sector 1-ID of the Advanced Photon Source, Argonne National Laboratory. Sector 1-ID operations and the work by J.-S.P. were supported by the Advanced Photon Source, a U.S. Department of Energy (DOE) Office of Science User Facility operated for the DOE Office of Science by Argonne National Laboratory under Contract No. DE-AC02-06CH11357. This support is gratefully acknowledged.

## References

1. Soboyejo WO, Srivatsan TS, *Advanced Structural Materials*. CRC Press; 2006. doi:10.1201/9781420017465

- 2. Chen L, Liu W, Song L. A multiscale investigation of deformation heterogeneity in additively manufactured 316L stainless steel. Materials Science and Engineering A. 2021;820. doi:10.1016/j.msea.2021.141493
- 3. Fecht H, Furrer D. Processing of Nickel-Base Superalloys for Turbine Engine Disc Applications. Adv Eng Mater. 2000;2(12):777-787. doi:10.1002/1527-2648(200012)2:12<777::AID-ADEM777>3.0.CO;2-R
- 4. Chen C, Huo Q, Zhang Z, et al. Effects of precipitate origin and precipitate-free zone development on the tensile creep behaviors of a hot-rolled Mg-13wt%Gd binary alloy. Mater Charact. 2021;178:111303. doi:10.1016/j.matchar.2021.111303
- 5. Shen Q, Wu X, Wei Q, et al. A strong-ductile niobium alloy enhanced by eutectic Nb2C. Materials Science and Engineering: A. 2023;882:145448. doi:10.1016/j.msea.2023.145448
- 6. Xia X, Peng Y, Zhang J, et al. Precipitation and growth behavior of  $\gamma'$  phase in Ni3Al-based superalloy under thermal exposure. J Mater Sci. 2019;54(20):13368-13377. doi:10.1007/s10853-019-03821-0
- 7. Seetharaman V, Sundararaman M, Krishnan R. Precipitation hardening in a PH 13-8 Mo stainless steel. Materials Science and Engineering. 1981;47(1):1-11. doi:10.1016/0025-5416(81)90034-3
- 8. Burtscher M, Klein T, Lindemann J, et al. An Advanced TiAl Alloy for High-Performance Racing Applications. Materials. 2020;13(21):4720. doi:10.3390/ma13214720
- 9. Tiwary CS, Kashiwar A, Bhowmick S, Hari Kumar KC, Chattopadhyay K, Banerjee D. Engineering an ultrafine intermetallic eutectic ternary alloy for high strength and high temperature applications. Scr Mater. 2018;157:67-71. doi:10.1016/j.scriptamat.2018.07.036
- 10. Vogel F, Wanderka N, Balogh Z, et al. Mapping the evolution of hierarchical microstructures in a Ni-based superalloy. Nat Commun. 2013;4(1):2955.

- doi:10.1038/ncomms3955
- 11. Chen YT, Chang YJ, Murakami H, et al. Hierarchical microstructure strengthening in a single crystal high entropy superalloy. Sci Rep. 2020;10(1):12163. doi:10.1038/s41598-020-69257-8
- 12. Dieter GE, Bacon D. Mechanical Metallurgy. Vol 3. McGraw-hill New York; 1986.
- 13. Product handbook of high performance nickel alloys. Special Metals, Huntington, WV, accessed May. 2015;22:2017.
- 14. Maity T, Singh A, Dutta A, Das J. Microscopic mechanism on the evolution of plasticity in nanolamellar  $\gamma$ -Ni/Ni5Zr eutectic composites. Materials Science and Engineering A. 2016;666:72-79. doi:10.1016/j.msea.2016.04.045
- Cortial F, Corrieu JM, Vernot-Loier C. Influence of heat treatments on microstructure, mechanical properties, and corrosion resistance of weld alloy 625.
   Metallurgical and Materials Transactions A. 1995;26(5):1273-1286.
   doi:10.1007/BF02670621
- 16. Maity T, Das J. High strength Ni–Zr–(Al) nanoeutectic composites with large plasticity. Intermetallics (Barking). 2015;63:51-58. doi:https://doi.org/10.1016/j.intermet.2015.04.002
- 17. Darling KA, Tschopp MA, VanLeeuwen BK, Atwater MA, Liu ZK. Mitigating grain growth in binary nanocrystalline alloys through solute selection based on thermodynamic stability maps. Comput Mater Sci. 2014;84:255-266. doi:10.1016/j.commatsci.2013.10.018
- 18. Li XL, He SM, Zhou XT, et al. Effects of rare earth yttrium on microstructure and properties of Ni-16Mo-7Cr-4Fe nickel-based superalloy. Mater Charact. 2014;95:171-179. doi:10.1016/j.matchar.2014.06.016
- 19. Du Z, Zhang W. Thermodynamic assessment of the Ni-Y system. J Alloys Compd. 1996;245(1-2):164-167. doi:10.1016/S0925-8388(96)02436-X
- 20. Du Z, Lü D. Thermodynamic modeling of the Co-Ni-Y system. Intermetallics.

- 2005;13(6):586-595. doi:10.1016/j.intermet.2004.09.013
- 21. Shevchenko MA, Ivanov MI, Berezutskii V V., Kudin VG, Sudavtsova VS.

  Thermodynamic properties of alloys of the Ni-Sc and Ni-Y systems. Russian
  Journal of Physical Chemistry A. 2014;88(6):897-902.

  doi:10.1134/S0036024414060284
- 22. Kosorukova T, Ivanchenko V, Firstov G, Noël H. Experimental reinvestigation of the Ni Zr system. Solid State Phenomena. 2013;194:14-20. doi:10.4028/www.scientific.net/SSP.194.14
- 23. Wang N, Li C, Du Z, Wang F. Experimental study and thermodynamic reassessment of the Ni-Zr system. *Calphad Comput Coupling Phase Diagrams Thermochem*. 2007;31(4):413-421. doi:10.1016/j.calphad.2007.07.001
- 24. Chen Q, Huang LH, Liu HS, Zheng F, Jin ZP. Isothermal sections of Al-Ni-Zr ternary system at 850 and 1050°C. J Phase Equilibria Diffus. 2013;34(5):390-402. doi:10.1007/s11669-013-0248-8
- 25. Wang CH, Chao KC, Fang TH, Stachiv I, Hsieh SF. Investigations of the mechanical properties of nanoimprinted amorphous Ni-Zr alloys utilizing the molecular dynamics simulation. J Alloys Compd. 2016;659:224-231. doi:10.1016/j.jallcom.2015.11.068
- 26. Morks MF, Fahim NF, Francis AA, Shoeib MA. Fabrication and characterization of electro-codeposited Ni/Zr-silicate composite coating. Surf Coatings Technol. 2006;201(1-2):282-286. doi:10.1016/j.surfcoat.2005.11.107
- 27. Acharya V, Ramesh S, Murthy GVS. Characterization of Intermetallic Precipitates in Ni-Base Alloys by Non-destructive Techniques. Superalloys. 2015. doi:10.5772/61119
- 28. Bradley, E.F. Superalloys: a technical guide. ASM International, United States, 1988.
- 29. Liu X, Yang S, Xiong H, et al. Experimental investigation of phase equilibria in the Co--Ni--Zr ternary system. International Journal of Materials Research.

- 2016;107(10):887-893.
- 30. Du J, Wen B, Melnik R, Kawazoe Y. First-principles studies on structural, mechanical, thermodynamic and electronic properties of Ni-Zr intermetallic compounds. Intermetallics. 2014;54:110-119. doi:10.1016/j.intermet.2014.05.021
- 31. Zhou YX, Hu MY, Yan P, Shi X, Chong XY, Feng J. A first-principles calculation of structural, mechanical, thermodynamic and electronic properties of binary Ni-Y compounds. RSC Adv. 2018;8(72):41575-41586. doi:10.1039/c8ra09383k
- 32. ASHBY MF, CEBON D. Materials selection in mechanical design. *Journal de Physique IV Proceedings*, 1993;03(C7):C7-1-C7-9. doi:10.1051/jp4:1993701
- 33. Baker H. *ASM Handbook: Alloy Phase Diagrams Volume 3*. ASM International Metalparts, Ohio, 1998.
- 34. Techniques | Advanced Photon Source. The advanced photon source. Accessed August 2, 2022. https://www.aps.anl.gov/Sector-1/1-ID/Techniques#tabs-5
- 35. Laliberte F. In-Situ Synchrotron X-Ray Investigation of Microstructure Evolution During Creep in Grade 91, Grade 92, and 14Ywt Oxide Dispersion Strengthened Steel. Ph.D. thesis. Rensselaer Polytechnic Institute; 2019;(April).
- 36. Toby BH, Von Dreele RB. GSAS-II: the genesis of a modern open-source all purpose crystallography software package. Journal of Applied Crystallography. 2013;46(2):544-549. doi:10.1107/S0021889813003531
- 37. Sansonetti JE, Martin WC. Handbook of basic atomic spectroscopic data. *Journal of physical and chemical reference data*. 2005;34(4):1559-2259. doi:10.1063/1.1800011
- 38. Buckley A. J. I. Goldstein, D. E. Newbury, P. Echlin, D. C. Joy, A. D. RomigJr, C. E. Lyman, C. Fiori & E. Lifshin 1992. Scanning Electron Microscopy and X-Ray Microanalysis. A Text for Biologists, Materials Scientists, and Geologists, 2nd ed. xviii + 820 pp. Ne. Geol Mag. 1993;130(3):402-403. doi:10.1017/S0016756800020276
- 39. Ware NG. Combined energy-dispersive–wavelength-dispersive quantitative electron microprobe analysis. X-Ray Spectrometry. 1991;20(2):73-79.

- doi:10.1002/xrs.1300200207
- 40. Schneider CA, Rasband WS, Eliceiri KW. NIH Image to ImageJ: 25 years of image analysis. Nature Methods. 2012;9(7):671-675. doi:10.1038/nmeth.2089
- 41. Ellingham HJT. Reducibility of oxides and sulfides in metallurgical processes. Journal of the Society of Chemical Industry. 1944;63:125-133.
- 42. Fukai Y. The Metal-Hydrogen System: Basic Bulk Properties. Vol 21. Springer Science & Business Media; 2006.
- 43. E9-19. Standard Test Methods of Compression Testing of Metallic Materials at Room Temperature. ASTM Book of Standards. 2019;(site 1):1-10. doi:10.1520/E0009-19.2
- 44. E209-18. Standard Practice for Compression Tests of Metallic Materials at Elevated Temperatures with Conventional or Rapid Heating Rates and Strain Rates. *ASTM B Standard*. 2000;00(2010):3-8. doi:10.1520/E0209-18.
- 45. Mezbahul-Islam M, Medraj M. Experimental study of the Cu-Ni-Y system at 700 °C using diffusion couples and key alloys. Journal of alloys and compounds. 2013;561:161-173. doi:10.1016/j.jallcom.2013.02.011
- 46. Villars P, Calvert LD. Pearson's Handbook of Crystallographic Data for Intermediate Phases. American Society of Metals, Cleveland, OH. Published online 1985.
- 47. Jain A, Ong SP, Hautier G, et al. Commentary: The Materials Project: A materials genome approach to accelerating materials innovation. APL Mater. 2013;1(1):011002. doi:10.1063/1.4812323
- 48. Generated using CrystalDiffract®: a powder diffraction program for Mac and Windows. CrystalMaker Software Ltd, Oxford, England (www.crystalmaker.com).
- 49. Giamei AF. Development of single crystal superalloys: {A} brief history. Adv Mater Process. 2013;171.

- 50. Reed RC, *The Superalloys: Fundamentals and Applications*. Cambridge University Press. 2008.
- 51. Vandersluis E, Ravindran C. Comparison of Measurement Methods for Secondary Dendrite Arm Spacing. Metallography, Microstructure, and Analysis. 2017;6(1):89-94. doi:10.1007/s13632-016-0331-8
- 52. Park JM, Kim TE, Sohn SW, et al. High strength Ni-Zr binary ultrafine eutectic-dendrite composite with large plastic deformability. Appl Phys Lett. 2008;93(3):2006-2009. doi:10.1063/1.2952755
- 53. Genau A, Ratke L. Morphological characterization of the Al–Ag–Cu ternary eutectic. International Journal of Materials Research. 2012;103(4):469-475. doi:10.3139/146.110652
- 54. Konrad CH, Glatzel U. Determination of oxygen diffusion along nickel/zirconia phase boundaries by internal oxidation. Oxidation of Metals. 2012;77(3-4):149-165. doi:10.1007/s11085-011-9278-y
- 55. Wang H, Li L, Zhu S, Xu Y, Ren N. Effect of water-based ultrasonic vibration on the quality of laser trepanned microholes in nickel super-alloy workpieces. J Mater Process Technol. 2019;272(February):170-183. doi:10.1016/j.jmatprotec.2019.04.034
- 56. Kohl HK, Peng K. Thermal stability of the superalloys Inconel 625 and Nimonic 86. Journal of Nuclear Materials. 1981;101(3):243-250. doi:10.1016/0022-3115(81)90166-5
- 57. Yang ZG, Stevenson JW, Paxton DM, Singh P, Weil KS. Materials Properties

  Database for Selection of High-Temperature Alloys and Concepts of Alloy Design
  for SOFC Applications. Pacific Northwest National Laboratory.

  2002;(November):4-78. doi:doi:10.2172/15010553
- 58. McCoy HE, King JF. Mechanical Properties of Inconel 617 and 618. Oak Ridge National Lab.(ORNL), Oak Ridge, TN (United States). 1985.

- 59. Guo Y, Wang B, Hou S. Aging precipitation behavior and mechanical properties of inconel 617 superalloy. Acta Metallurgica Sinica (English Letters). 2013;26(3):307-312. doi:10.1007/s40195-012-0249-3
- 60. Clickner CC, Ekin JW, Cheggour N, et al. Mechanical properties of pure Ni and Ni-alloy substrate materials for Y-Ba-Cu-O coated superconductors. Cryogenics (Guildf). 2006;46(6):432-438. doi:10.1016/j.cryogenics.2006.01.014
- 61. Cinoglu IS, Charbal A, Vermaak N. Towards exploiting inelastic design for Inconel 625 under short-term cyclic loading at 600°C. Mechanics of Materials. 2020;140:103219. doi:10.1016/j.mechmat.2019.103219
- 62. MacKay RA, Nathal MV.  $\gamma'$  coarsening in high volume fraction nickel-base alloys. Acta Metallurgica et Materialia. 1990;38(6):993-1005. doi:10.1016/0956-7151(90)90171-C
- 63. Ges A, Fornaro O, Palacio H. Long term coarsening of  $\gamma'$  precipitates in a Ni-base superalloy. J Mater Sci. 1997;32(14):3687-3691. doi:10.1023/A:1018694716756
- 64. McLean D. Predicting growth of  $\gamma$ 'in nickel alloys. Metal Science. 1984;18(5):249-256. doi:10.1179/030634584790420113
- 65. Andrews RN, Serio J, Muralidharan G, Ilavsky J. An in situ USAXS–SAXS–WAXS study of precipitate size distribution evolution in a model Ni-based alloy. Journal of Applied Crystallogy. 2017;50(3):734-740. doi:10.1107/S1600576717006446
- 66. Armstrong W. Tentative Equilibrium Diagram for the Nickel-rich End of the Nickel-Zirconium System. Ph.D. thesis, Oregon State College, 1960;(June).
- 67. Fleischer RL. Substitutional solution hardening. Acta Metallurgica. 1963;11(3):203-209. doi:10.1016/0001-6160(63)90213-X
- 68. Rehman H. Solid Solution Strengthening and Diffusion in Nickel- and Cobalt-Based Superalloys. Ph.D. thesis, Friedrich-Alexander-University Erlangen-Nuremberg (FAU); 2016. https://opus4.kobv.de/opus4-fau/frontdoor/index/index/docId/7407

- 69. Friedel J, Smoluchowski R. Dislocations. Phys Today. 1957;10(7):36-39. doi:10.1063/1.3060437
- 70. Labusch R. A Statistical Theory of Solid Solution Hardening. Physica status solidi (b). 1970;41(2):659-669. doi:10.1002/pssb.19700410221
- 71. Leyson GPM, Curtin WA. Friedel vs. Labusch: the strong/weak pinning transition in solute strengthened metals. Philosophical Magazine. 2013;93(19):2428-2444. doi:10.1080/14786435.2013.776718
- 72. Wang MX, Zhu H, Yang GJ, Liu K, Li JF, Kong LT. Solid-solution strengthening effects in binary Ni-based alloys evaluated by high-throughput calculations.

  Materials & Design. 2021;198:109359. doi:10.1016/j.matdes.2020.109359
- 73. Spader D, Maciejewski K, Ghonem H. Distribution of Grain Boundary Carbides in Inconel 617 Subjected to Creep at 900 °C and 950 °C. Metall Mater Trans A Phys Metall Mater Sci. 2020;51(7):3473-3487. doi:10.1007/s11661-020-05798-x